# Role of Interactions of Boundary Conditions and Baroclinic Vorticity in the Instability of Thermally Stratified Spinup in a Cylinder

by

Aditya Deepak Kher

A Thesis Presented in Partial Fulfillment
of the Requirements for the Degree
Master of Science

Approved November 2011by the
Graduate Supervisory Committee:

KangPing Chen, Chair
Huei-Ping Huang
Marcus Herrmann

ARIZONA STATE UNIVERSITY

December 2011

ABSTRACT

A numerical study of incremental spin-up and spin-up from rest of a thermally-stratified fluid enclosed within a right circular cylinder with rigid bottom and side walls and stress-free upper surface is presented. Thermally stratified spin-up is a typical example of baroclinity, which is initiated by a sudden increase in rotation rate and the tilting of isotherms gives rise to baroclinic source of vorticity. Research by (Smirnov *et al.* [2010*a*]) showed the differences in evolution of instabilities when Dirichlet and Neumann thermal boundary conditions were applied at top and bottom walls. Study of parametric variations carried out in this dissertation confirmed the instability patterns observed by them for given aspect ratio and Rossby number values ($\varepsilon > 0.5$). Also results reveal that flow maintained axisymmetry and stability for short aspect ratio containers independent of amount of rotational increment imparted. Investigation on vorticity components provides framework for baroclinic vorticity feedback mechanism which plays important role in delayed rise of instabilities when Dirichlet thermal BCs are applied.

ACKNOWLEDGEMENTS

I acknowledge the Ira A. Fulton High Performance Computing Initiative at Arizona State University for providing HPC and visualization resources. I appreciate help and support given by Department of Mechanical Engineering, particularly Dr. Sharon Yee, Dr. Patrick Phelan. I also thank Dr. Hermann and Dr. Huang for serving on my master's thesis committee. I would like to express my deepest gratitude to my advisor Dr. KangPing Chen and mentor Dr. Rafael Pacheco for their continuous guidance and encouragement.

TABLE OF CONTENTS

LIST OF FIGURES

LIST OF TABLES

# Chapter 1

## INTRODUCTION

One of the aspects of studying rotating fluids is to explore influence of earth's rotation on large scale geophysical flows. This is the list of some authors ([Linden & van Heijst, 1984; Allen, 1973; Boyer *et al.*, 2009; Garrett *et al.*, 1993; Manley & Hunkins, 1985; McWilliams, 1985; Olson, 1991; Mouling & Flór, 2004; Ungarish & Mang, 2003; Hallworth *et al.*, 2001; Mahalov *et al.*, 2000; Hunt *et al.*, 2005]), who dealt with spin-up problem in regards to geophysical flows. Spin-up is the process through which initially rotating fluid adjusts itself, when subjected to sudden increase in angular speed (Thomas & Rhines [2002]); whereas stratification is formation of density profile (in this case linear) in the fluid due to variation in temperature (or salinity). Examples of such geophysical flows are wind driven surface flow; ocean currents in coastal regions; geophysical vortical flows e.g. ocean rings, Arctic eddies; and the polar vortices in the atmosphere. My research focuses on time dependent development of instabilities due to spin-up. Non-linear spin-ups are those in which Rossby number (defined as $\varepsilon = \frac{\Delta\Omega}{\Omega}$ i.e. ratio of change in angular velocity to final angular velocity) is ($\varepsilon$ $O(1)$). This prevents one from neglecting rotational effects while solving Navier Stokes equations (Greenspan [1968]).

Records of developments in spin-up of homogeneous and stratified fluids can be found in (Benton & Clark [1974]) and (Duck & Foster [2001]). Various numerical and experimental studies on spin-up problems showed that two processes principally govern spin-up phenomenon. First one is viscous dissipation of angular momentum from the sidewall, where the imposed no-slip boundary condition at the sidewall and sidewall itself assist the spin-up of fluid. The second process is advection of angular momentum caused by pumping of fluid through Ekman layer on top and bottom surfaces. In case at hands shear free surface at top prohibits formation of Ekman layer at top boundary. (Flór *et al.* [2002]) found that curvature of isopycnals (constant density lines) leads to diffusive mass transport with radial component and concomitant Sweet-Eddington azimuthal flow.

Thus secondary flows caused by Ekman layer transport influence the spin-up process. In homogeneous fluids the Ekman pumping occurs at time scale of $E^{-1/2}\Omega^{-1} = h/(\nu\Omega)^{1/2}$, where Ekman number is $E = \nu/\Omega h^2$. Here $h$ is fluid depth and $\nu$ is kinematic viscosity of fluid. In stratified fluids the spin-up time is influenced by buoyancy frequency $N$. Stratification weakens Ekman suction. Upwelling is observed as heavy fluid near the bottom is forced radially outwards and it rises at sidewall forming corner regions where surfaces of constant density are deformed. Upwelling promotes the formation of sidewall boundary layers. In case of non-linear spin-up this tends to reduce the spin-up time as sidewall boundary layers assist in advection of angular momentum from sidewall to interior of the fluid domain. Deformation of isopycnals may trigger baroclinic instabilities responsible for inertial oscillations and vertical vortex structures. These eddies expedite the spin-up process by enhancing the transport of angular momentum (Greenspan [1980]). Such instabilities broke axisymmetry in case of salt stratified spin-up experiments conducted by (Kanda [2004]), (Flór *et al.* [2004]) and (Smirnov *et al.* [2005]). For incremental spin-up (Kanda [2004]) found that viscous effects become important at sidewall indicated by delay in the instability.

Numerical and experimental treatment of this problem had been limited mostly to axisymmetric regime. Recently (Smirnov *et al.* [2010*a*]) studied the role of thermal Boundary Conditions (BCs) of at horizontal walls. They conducted numerical simulations to analyse effects of Dirichlet and Neumann thermal BCs on development of axisymmetry breaking instabilities. In both cases instabilities were initiated by horizontal (barotropic)and vertical (baroclinic) shears. In case of Dirichlet temperature BC at top and bottom boundaries of fluid, initial instabilities were suppressed for some rotations due to imposed stratification by top and bottom thermal BCs. They found that baroclinic instabilities grew again and broke the axisymmetry, leading to formation of eddies at late times. In case of Neumann thermal BCs at top and bottom boundaries flow lost the axisymmetry immediately along with growth of instabilities with no sign of suppression. Internal waves were also generated as axisymmetry was lost along with formation of eddies.

Hence it is clear that due to weakened stratification in case of Neumann thermal BCs offers less resistance to instabilities. Questions arised as Dirichlet BCs are applied

(stratification was imposed) the instabilities were suppressed initially, so why did they rise again after some rotations leading to loss of axisymmetry ? Are these instabilities specific to space parameters ? How do these instabilities behave when subjected to spin-up from rest ? Intending to find answers to these questions a series of numerical simulations was carried out. Results of (Smirnov *et al.* [2010*a*]) are reproduced and extended for different aspect ratios and rotation rates. Both Dirichlet and Neumann thermal Boundary conditions (BC) were studied. Based on the fact that tilting of isotherms gives rise to baroclinic source of vorticity which enhances the circulation in the vertical plane; this dissertation explores dynamics of baroclinic vorticity in the wake of non-linear spin-up. Numerical simulations conducted in this research provide framework for development of interactive mechanisms causing delayed instability. Study of parametric variations allows one to identify any particular factor that affects this kind of spin-up. In next chapter information of governing equations is provided in one subsection while the other subsection deals with numerical methods, code validation etc. The third chapter handles the observations and results, followed by fourth chapter on conclusions giving brief summary of inferences.

Chapter 2

# GOVERNING EQUATIONS AND NUMERICAL METHOD

## 2.1 Governing equations

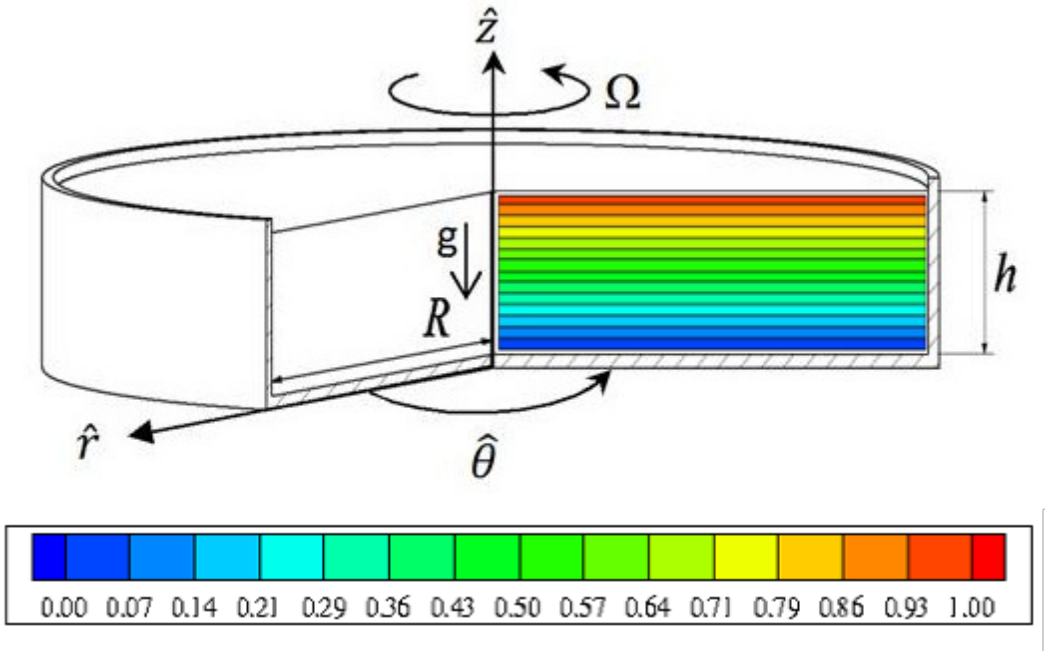


Figure 2.1: Schematic of the Numerical simulations set-up. The cross section along $\hat{r}-\hat{z}$ plane at $\hat{\theta}=0$ shows the isotherms at time $\hat{t}=0$ depicting initial temperature profile used. Below is the color scheme used to show 15 contour levels of non-dimensional temperature $\Theta \in (0-1)$ with corresponding values used in all isotherm plots.

The numerical simulations are performed in cylindrical co-ordinate system with $\hat{\boldsymbol{r}} = (\hat{r}, \hat{\theta}, \hat{z})$ as radial, azimuthal and vertical directions with $\boldsymbol{e}_r$, $\boldsymbol{e}_\theta$, $\boldsymbol{e}_z$ as unit vectors in respective directions. The incompressible Newtonian fluid of density $\rho$ is assumed to be bounded by a right circular cylinder of height $h$ and radius $R$ so that aspect ratio can be defined as $\Gamma = \frac{R}{h}$. Cylinder rotates about $\hat{z}$-axis in counter-clockwise direction as shown in the figure 2.1. The gravity $g$ acts along the axis of rotation so that $-e_z$ is unit vector in the direction of gravity. Initially cylinder rotates with angular speed of $\Omega_i$. At time $\hat{t}=0$ angular speed of rotation is increased by $\Delta\Omega$ to a new rotation rate $\Omega$ such that $\Omega_i = \Omega(1-\varepsilon)$. The

flow is described by velocity vector $\hat{\boldsymbol{u}}$ which has three components $\hat{u}_r$ , $\hat{u}_\theta$ and $\hat{u}_z$ in radial, azimuthal and vertical directions respectively.

Following are the properties of the fluid used in simulations :

| Property | Expression | Value | Units |
|---|---|---|---|
| Temperature drop | $\Delta T$ | 20 | °C |
| Mean Density | $\rho_0$ | 1.0 | $g/cm^3$ |
| Gravitational Acceleration | g | 981 | $cm/s^2$ |
| Kinematic Viscosity | $\nu$ | 0.01 | $cm^2$/s |
| Thermal Diffusivity | $\kappa$ | $1.46 \times 10^-3$ | $cm^2/s$ |
| Coefficient of Thermal Expansion | $\alpha$ | $2.86 \times 10^{-4}$ | $(°C)^{-1}$ |
| Buoyancy Frequency | $N$ | 0.97 | $rad/s$ |

Table 2.1: Properties of fluid used in simulations.

The full governing equations in vector form in rotational frame of reference are given as follows :

$$\hat{\boldsymbol{\nabla}} \cdot \hat{\boldsymbol{u}} = 0 \tag{2.1a}$$

$$\frac{D\hat{\boldsymbol{u}}}{D\hat{t}} + 2\boldsymbol{\Omega} \times \hat{\boldsymbol{u}} = -\frac{1}{\rho_0}\hat{\boldsymbol{\nabla}}\hat{p} - \frac{\rho}{\rho_0} g e_z + \frac{\rho}{\rho_0}\Omega^2 \hat{r} e_r + \nu \hat{\nabla}^2 \hat{u} \tag{2.1b}$$

$$\frac{D\hat{\boldsymbol{T}}}{D\hat{t}} = \kappa \hat{\nabla}^2 \hat{T} \tag{2.1c}$$

Boussinesq approximation is used so that mean density $\rho_0$ can be used to avoid it interfering with non-linear terms. This is possible because maximum temperature difference applied is 20°C so that variation in density due to temperature can be neglected while calculating rates of change of momentum due to acceleration (Gill [1982]). In equation 2.1, $D/D\hat{t}$ denotes substantial derivative given by $\partial/\partial\hat{t} + \hat{\boldsymbol{u}} \cdot \hat{\boldsymbol{\nabla}}$; where $\hat{\boldsymbol{\nabla}}$ is vector differential operator. $\hat{p}$ and $\hat{T}$ are total pressure and total temperature functions respectively. The background temperature $T_b$ of thermal stratification and buoyancy frequency $N$ are defined as follows :

$$T_b(z) = T_0 + \frac{\Delta\hat{T}}{h}\hat{z}, \qquad \text{and} \qquad N^2 = \alpha g \frac{\Delta\hat{T}}{h}$$

$$\therefore\ T_b(z) = T_0 + \frac{N^2}{\alpha g} z$$

$N^2 \geq 0$ implies that initially fluid is stably stratified. $T_0$ and $T_0 + \Delta\hat{T}$ are the initial temperatures at top and bottom of the fluid domain respectively. In further analysis reduced pressure $\hat{P}$ given by $\hat{P} = \hat{p} + \rho_0 g\hat{z} - \rho_0(\Omega\hat{r})^2/2$ are used respectively. At the side wall, no-slip boundary conditions are used for velocity and insulated boundary condition is used for temperature. These can be represented mathematically as :

$$\hat{u}_r = \hat{u}_z = 0, \hat{u}_\theta = -\Delta\Omega\hat{r}, \hat{T} = T_0 + \frac{\Delta\hat{T}}{h}\hat{z} \qquad \text{at} \qquad \hat{t} = 0, \tag{2.2a}$$

$$\hat{u}_r = \hat{u}_z = \hat{u}_\theta = 0 \qquad \text{at} \qquad \hat{z} = 0, \tag{2.2b}$$

$$\frac{\partial \hat{u}_r}{\partial \hat{z}} = \frac{\partial \hat{u}_\theta}{\partial \hat{z}} = \hat{u}_z = 0 \qquad \text{at} \qquad \hat{z} = h, \tag{2.2c}$$

$$\hat{u}_r = \hat{u}_\theta = \hat{u}_z = 0, \frac{\partial \hat{T}}{\partial \hat{r}} = 0 \qquad \text{at} \qquad \hat{r} = R. \tag{2.2d}$$

Following table shows characteristic parameters defined to non-dimensionalize the governing equations. Additionally variable $\Theta$ is used to denote non-dimensional temperature given by $\Theta = (\hat{T} - \hat{T}_0)/\Delta T$, with total initial temperature difference $\Delta\hat{T}$ between top and bottom boundaries of cylinder as temperature scale. Substituting these values, dividing both sides

| Parameter | Expression |
|---|---|
| Length | $h$ |
| Time | $\Omega^{-1}$ |
| Velocity | $\Omega h$ |
| Pressure | $\Omega^2 h^2 \rho_0$ |
| Temperature | $\Delta T$ |

Table 2.2: Characteristic Parameters Used for Non-dimensionalization

by $\Omega^2 h$ and for simplicity, dropping the hat mark on variables to indicate non-dimensional form, these equations are written as follows.

$$\boldsymbol{\nabla} \cdot \boldsymbol{u} = 0 \tag{2.3a}$$

$$\frac{\partial \boldsymbol{u}}{\partial t} + (\boldsymbol{u} \cdot \boldsymbol{\nabla}\boldsymbol{u}) = -\boldsymbol{\nabla} P + \left(B^2 \boldsymbol{e}_z - FB^2 r \boldsymbol{e}_r\right)\Theta + 2(u \times e_z) + E\nabla^2 u \tag{2.3b}$$

$$\frac{\partial \Theta}{\partial t} + (u \cdot \nabla\Theta) = \frac{E}{\sigma}\nabla^2\Theta \tag{2.3c}$$

The boundary and initial conditions are written as :

$$\text{At } t = 0, u_r = u_z = 0, u_\theta = -\varepsilon r, \Theta = z \tag{2.4a}$$

$$\text{At } z = 0, u_r = u_\theta = u_z = 0 \tag{2.4b}$$

$$\text{At } z = 1, \frac{\partial u_r}{\partial z} = \frac{\partial u_\theta}{\partial r} = u_z = 0 \tag{2.4c}$$

$$\text{At } r = \Gamma, u_r = u_\theta = u_z = 0, \frac{\partial \Theta}{\partial r} = 0 \tag{2.4d}$$

Following table shows the parameters that are used in above equations.

To sum-up parameter space is governed by parameters in table 2.3. Here Prandtl num-

| Parameter | Expression |
|---|---|
| Rossby Number | $\varepsilon = \Delta\Omega/\Omega$ |
| Ekman Number | $E = \nu/\Omega h^2$ |
| Aspect Ratio | $\Gamma = R/h$ |
| Burger number | $B = N/\Omega$ |
| Rotational Froude Number | $F = \Omega^2 h/g$ |
| Prandtl Number | $\sigma = \nu/\kappa$ |

Table 2.3: Dimensionless Parameters Used

ber stands for relative importance of momentum diffusion and thermal diffusion; Froude number relates Centrifugal and gravitational accelerations whereas stratification parameters stores information about Buoyancy force and Coriolis force. Finally Ekman number grossly measures ratio of viscous acceleration and Coriolis force (Benton & Clark [1974]). Table 2.4 gives detailed idea of parameter space explored:

As mentioned above the Temperature boundary conditions for 2 series are :

For Neumann BC

$$\text{At } z = 0, 1 \qquad \frac{\partial \Theta}{\partial z} = 0, \tag{2.5}$$

For Dirichlet BC

$$\text{At } z = 0, \qquad \Theta = 0, \qquad \text{At } z = 1, \qquad \Theta = 1, \tag{2.6}$$

| *Dimensional parameters* | *Expression* | *Values* |
|---|---|---|
| Height | $h$ [cm] | 6 |
| Radius | $R$ [cm] | 6–20 |
| Final rotation rate | $\Omega$ [rad/s] | 0.384 |
| Rotation rate increment | $\Delta\Omega$ [rad/s] | 0.279 – 0.384 |
| Ekman layer depth | $\delta = (\nu/\Omega)^{1/2}$ [cm] | 0.16 |
| Rossby deformation radius | $Ro = Nh/\Omega$ [cm] | 15.625 |
| Spin-up time | $\tau_E = h/(\nu\Omega)^{1/2}$ [s] | 97 |
| Viscous time | $\tau_\nu = R^2/\nu$ [s] | $3,600 - -40,000$ |
| Characteristic velocity | $U = \Delta\Omega R$ | $1.67 - -7.68$ |
| *Nondimensional parameters* | | |
| Aspect ratio | $\Gamma = h/R$ | 1–3.3 |
| Burger number | $B = N/\Omega$ | 2.52 |
| Ekman number | $E = \nu/\Omega h^2$ | $7.20 \times 10^{-4}$ |
| Ekman layer depth | $\delta_E = \delta/h$ | $2.69 \times 10^{-2}$ |
| Froude number | $F = \Omega^2 h/g$ | $9.0 \times 10^{-4}$ |
| Prandtl number | $\sigma = \nu/\kappa$ | 6.85 |
| Reynolds number | $Re_\delta = U\delta/\nu$ | $27.78 - -122.8$ |
| Reynolds number rotational | $Re_\Omega = UR/\nu$ | $1,004 - -15,360$ |
| Rossby number | $\varepsilon = \Delta\Omega/\Omega$ | $0.5 - -1$ |
| Spin-up time | $t_E = \Omega\tau_E/2\pi$ | 5.9 rotations |
| Viscous time | $t_\nu = \Omega R^2/(2\pi\nu)$ | 2,500 rotations |

Table 2.4: Range of parameters used in the simulations.

In order to sort and monitor the contributions of different terms from momentum equation, method described in (Verzicco *et al.* [1997]) and adopted by (Smirnov *et al.* [2010*a*]) is followed. Accordingly variables in equation (2.3) are decomposed into axisymmetric and non-axisymmetric parts as shown below in equation 2.7. $\bar{q}(r,z)$ is the axisymmetric part representing mean flow (hence independent of $\theta$), where as $q'(r,\theta,z)$ is the non-axisymmetric part representing the flow perturbations.

$$q(r,\theta,z) = \bar{q}(r,z) + q'(r,\theta,z), \tag{2.7}$$

with,

$$\bar{q}(r,z) = \frac{1}{2\pi}\int_0^{2\pi} q(r,\theta,z)\,\mathrm{d}\theta. \tag{2.8}$$

Next kinetic energy equation is obtained in terms of these azimuthal disturbances by taking velocity $\boldsymbol{u}$ as quantity $q$, putting it into equation (2.3)b, taking dot product with $\boldsymbol{u}'$ and

integrating over entire volume of domain $V$.

$$\begin{aligned}\frac{\mathrm{d}e}{\mathrm{d}t} = \frac{\mathrm{d}}{\mathrm{d}t}\int_V \frac{1}{2}|\boldsymbol{u}'|^2 \mathrm{d}V &= -\int_V \boldsymbol{u}' \cdot (\boldsymbol{u}' \cdot \boldsymbol{\nabla}\bar{\boldsymbol{u}})\mathrm{d}V + B^2 \int_V \Theta u_z' \mathrm{d}V \\ &\quad -FB^2 \int_V \Theta r u_r' \mathrm{d}V - E\int_V |\nabla \boldsymbol{u}'|^2 \mathrm{d}V, \qquad (2.9) \\ &= \sum_{i=1}^{4} h_i.\end{aligned}$$

The LHS of integral equation (2.9) is the kinetic energy growth rate of the azimuthal perturbation. Whereas its RHS comprises of 4 $H_i$ terms which represent (1) $h_1$: barotropic contribution due to shear of the mean axisymmetric flow; (2) $h_2$: conversion of gravitational potential energy (baroclinic term); (3)$h_3$: conversion of centrifugal potential energy; (4) $h_4$: viscous dissipation. This way azimuthal perturbations are characterized through total kinetic energy of the perturbations of flow evolution. Time evolution of kinetic energy in the $m^{th}$ Fourier mode of solution is plotted, with help of Fourier analysis of velocity field. This enables one to identify the most unstable wave number $m$ as mode with highest growth rate.

$$e_m = \frac{1}{2}\int_{r=0}^{r=\Gamma}\int_{z=0}^{z=2} \boldsymbol{u}_m \cdot \boldsymbol{u}_m^*.\, r\, dr\, dz \qquad (2.10)$$

In addition to this following equation governs the evolution of vorticity.

$$(\partial_t + \boldsymbol{u}\cdot\nabla)\boldsymbol{\omega} = \boldsymbol{\omega}\cdot\nabla\boldsymbol{u} + B^2\nabla\Theta\times\boldsymbol{e}_z + E\,\nabla^2\boldsymbol{\omega}, \qquad (2.11)$$

Here first term on the RHS indicates vorticity generation by stretching and tilting, the second term accounts for baroclinic vorticity and the third term represents vorticity diffusion. The focus is on the production of baroclinic vorticity at the walls which can be expressed in its components as as

$$\nabla\Theta\times\boldsymbol{e}_z = \left(\frac{1}{r}\frac{\partial}{\partial\theta}\boldsymbol{e}_r - \frac{\partial}{\partial r}\boldsymbol{e}_\theta\right)\Theta \qquad (2.12)$$

## 2.2 Numerical method and code verification

numerical method used by (Smirnov *et al.* [2010*a*]) was applied so that results can be analyzed without computational differences. In other words, staggered grid is used to discretize the governing equations (2.3) having velocities at the faces and all scalar quantities at center of the grid cell. Viscous and advective terms in the equations system are discretized with

second-order central difference approximation. Fractional step method is implemented to solve the system. Pressure-Poisson equation which accounts for incompressibility is solved using, trigonometric expansions in the azimuthal direction and tensor product method in other two directions. Time step is obtained by third-order Runge-Kutta method with explicit treatment of non-linear terms and implicit treatment for viscous terms. Involvement of explicit treatment imposes stability limit of CFL $< \sqrt{3}$. Where CFL that is Courhant, Friedrichs, Lewy number and is locally expressed as,

$$CFL = (|u_r|/\delta r + |u_\theta|/(r\delta\theta) + |u_z|/\delta z)\delta t \tag{2.13}$$

where, velocities are calculated as average at center of each cell. The smallest local $\delta t$ is found from CFL $\leq 1.5$ and is used as time advancement. This code has been used by ([Verzicco & Orlandi, 1996; Verzicco & Camussi, 1997; Verzicco *et al.*, 1997; Smirnov *et al.*, 2010*a*,*b*; Pacheco *et al.*, 2011]) on many problems which involved convection in rotating cylinder. These simulations allow one to set the grid resolution of $n_r \times n_\theta \times n_z = 351(251)(151) \times 96 \times 151$ at aspect ratios of $\Gamma = 3.3, 2.0, 1.0$ respectively. For reference code verification done in (Smirnov *et al.* [2010*a*]) is presented here, where they compared results of simulation with experimental results of ref. (Hyun *et al.* [1982]) for spin-up with thermal stratification. As seen in the figure 2.2, numerical solution of azimuthal velocity is found to be in good agreement with the experimental results. Furthermore to check grid sensitivity (Smirnov *et al.* [2010*a*]) did one simulation with $n_r \times n_\theta \times n_z = 351 \times 96 \times 151$ and verified the grid independence by running the same case on finer grid of $n_r \times n_\theta \times n_z = 601 \times 192 \times 251$.

Above figure 2.3 shows the time evolution of three velocity components at $(\theta, r, z) = (0, 0.5, 0.1)$ for two sets of grids. Up to ($\tau < 20$) the flow remains axisymmetric with both curves for each component overlapping each other. As perturbations increase the curves start showing slight departure from each other. At later times the two curves show larger differences. The reason behind these differences in values lies in the fact that perturbations are triggered by truncational errors, which in-turn depend upon the implemented grid. Hence as perturbations grow the three dimensional evolution of flow can show slight dif-

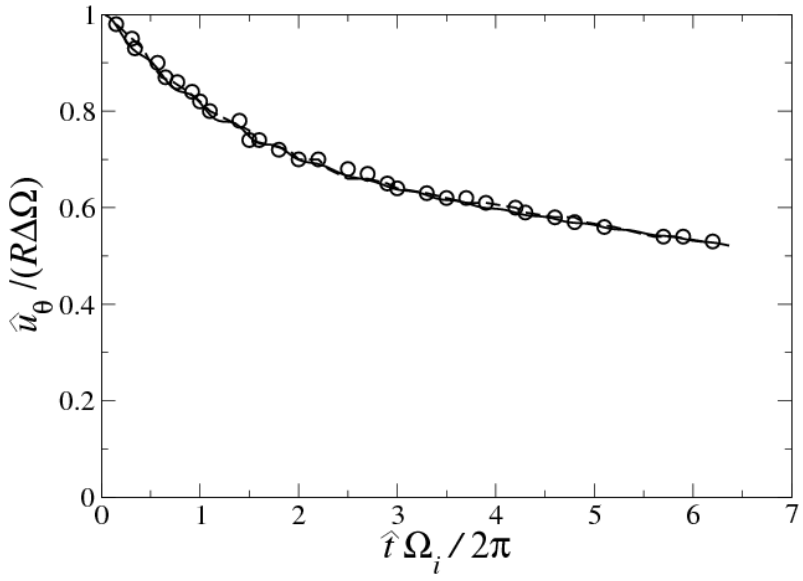


Figure 2.2: Comparison of stratified spin-up experiments with numerical simulations for the azimuthal velocity $\hat{u}_\theta$. Thermal stratification: Parameters: $2H = 6$cm, $R = 9.5$cm, $N = 0.97\text{s}^{-1}$, $\Omega = 0.384\text{s}^{-1}$, $S\Gamma^{-1}(= NH/2\Omega_i R) = 0.49$, $E(= \nu/2\Omega_i H^2) = 7.24 \times 10^{-4}$, $\varepsilon(= \Delta\Omega/\Omega_i) = 0.222$ and $\Omega_i = 0.314\text{s}^{-1}$. The vertical and radial locations are at the mid-depth $\hat{z} = H$ and $\hat{r}/R = 0.64$. The circles ($\circ$) correspond to the laser-Doppler measurements of (Hyun *et al.* [1982]) and the solid lines (——) to our numerical simulations.

ferences depending on grid. Nevertheless it can be noted that overall trend remains almost same for both grids. The objective of this research is to investigate causes of delayed instabilities in Dirichlet cases. It is confirmed that grid refinement did not cause much variation in time of evolution of instabilities. Hence with respect to objective, these differences are sufficiently low to assume the grid independence. Hence the coarser grids of $n_r \times n_\theta \times n_z = 351(251)(151) \times 97 \times 151$ for respective aspect ratios of 3.3,2.0 and 1.0. are implemented for all simulations performed.

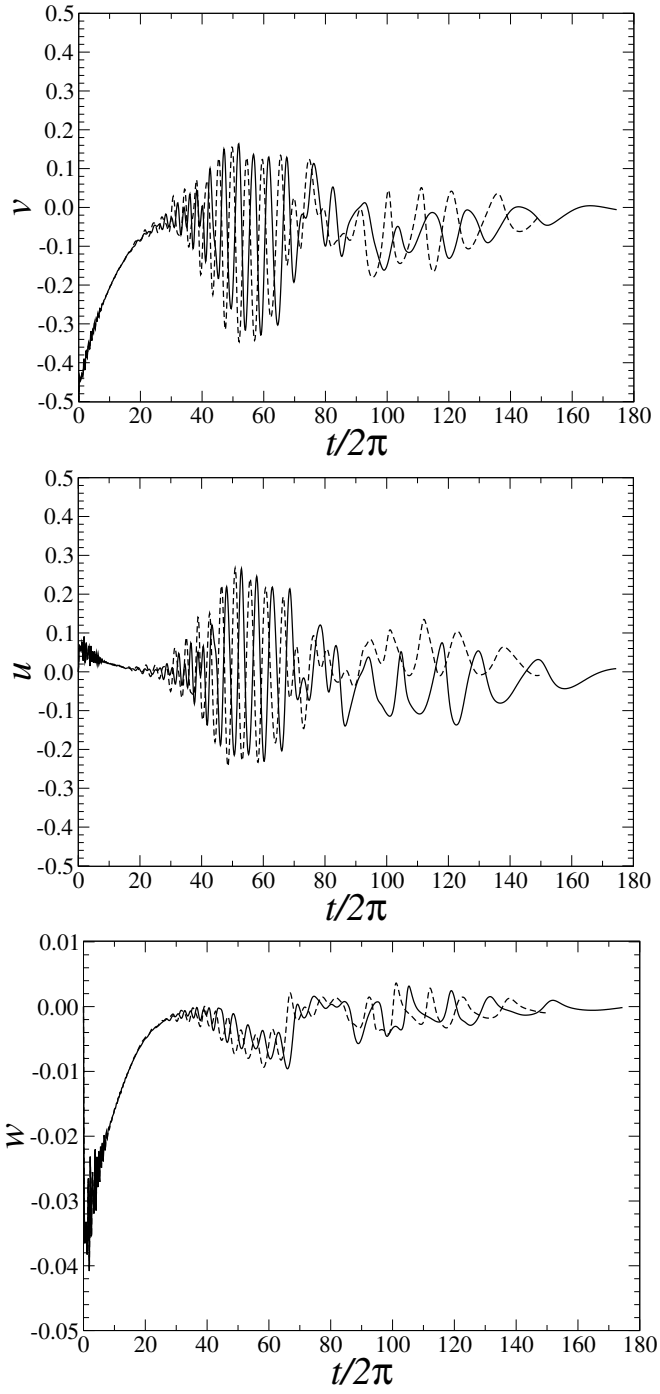


Figure 2.3: Comparison of time evolution of three velocity components at position $(\theta, r, z) = (0, 0.5, 0.1)$ with $(96 \times 351 \times 151)$—— ; and $(192 \times 601 \times 251)$ – – grids

Chapter 3

# RESULTS

In this section observations for both Neumann and Dirichlet series are put forth. It deals with response of spin-up system to variation of Aspect ratio and Rossby number. The numerical simulations were carried out for three different aspect ratios $\Gamma = 1.0, 2.0, 3.3$. For each value of aspect ratio three cases of Rossby number $\varepsilon = 0.5, 0.73 and 1.0$ are studied. Results are presented in following sequence:

- Stability regime for both Neumann and Dirichlet cases.
- Unstable cases
- Analysis of baroclinic vorticity dynamics for unstable cases.

## 3.1 Stability regime for both Neumann and Dirichlet cases

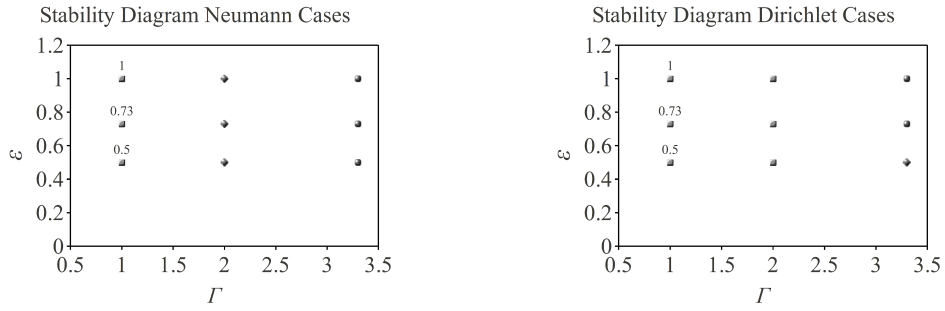


Figure 3.1: Stability regimes for Neumann BC cases. Left column: Neumann cases and Right column Dirichlet cases. $--\Box--$ indicates the cases which maintained axisymmetry and stability. $--\Diamond--$ stands for the cases which lost axisymmetry initially but maintained the stability and retained axisymmetry at the end. $--\circ--$ are the the cases where axisymmetry was completely lost and instability prevailed.

Stability of flow is recognized from plots of Fourier energy modes in equation 2.10. In these plots as energy curve of $m^{th}$ mode approaches that of $(m = 0)$ i.e. mean current mode, flow starts showing signs of loss of axisymmetry. Flow is defined to be unstable if any of $(m \neq 0)$ mode overtakes $(m = 0)$ *i.e.* mean current mode.

Figure 3.2 shows the sample m-energy mode plots at labeled values of $\varepsilon$ and $\Gamma$. It is found

(a) $\varepsilon = 1.0, \Gamma = 1.0$

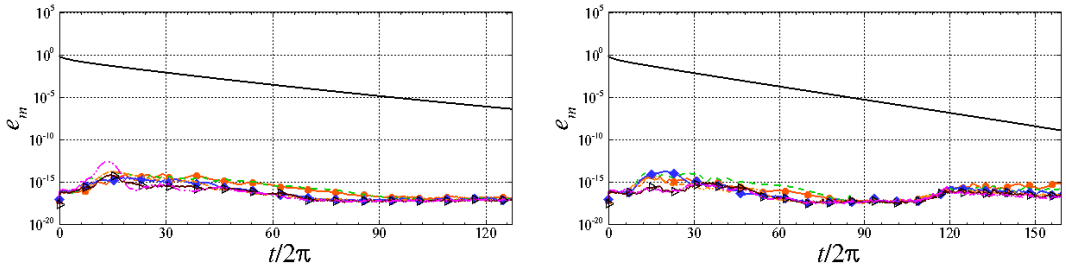


(b) $\varepsilon = 1.0, \Gamma = 2.0$

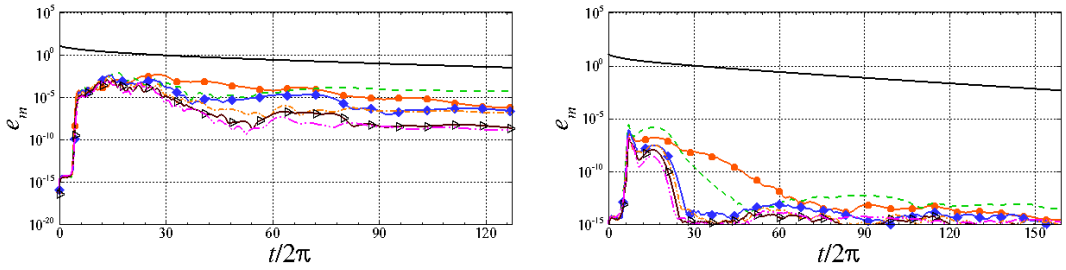


Figure 3.2: Time evolution of different energy modes $e_m$ at labeled aspect ratios. $\Gamma$. The figures in the left column correspond to the spin-up with Neumann thermal BCs, and those in the right column to the Dirichlet thermal BCs. $m = 0$ (—— black); $m = 1$ (–○– red); $m = 2$ (– – green); $m = 3$ (–◇– blue); $m = 4$ (–·– orange); $m = 5$ (–▷– brown); $m = 6$ (–· ·– magenta).

that flow remains stable for $\varepsilon = 0.5, 0.73, 1.0$ and aspect ratio of $\Gamma = 1.0, 2.0$. It can be seen that for Neumann BC cases at $\Gamma = 2.0$ and $\varepsilon = 0.5, 0.73, 1.0$ the non-axisymmetric modes gain some energy, but they remain below the energy curve of mean current flow through out the simulation. Although initially for $\Gamma = 2.0$ at all Rossby numbers there was a slight loss of axisymmetry in bottom half of the tank. Figure 3.3 illustrates this. It shows vector plots of baroclinic vorticity with temperature $\Theta$ in the background. It shows clearly that axisymmetry is regained after $(t/2\pi) = 50$

(a) $z = 0.008$

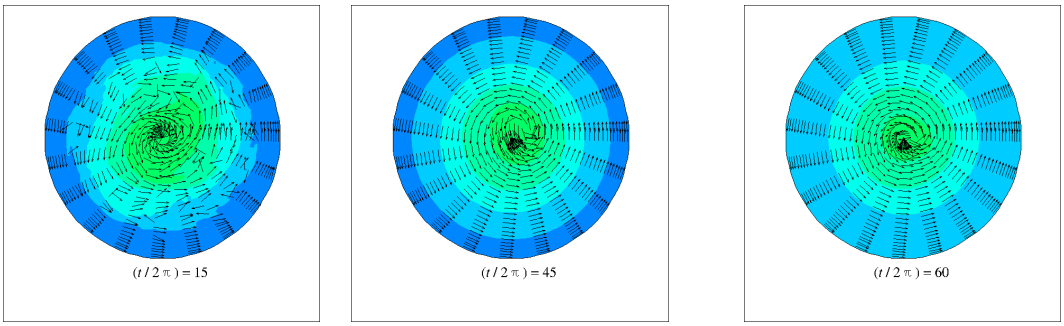


(b) $z = 0.5$

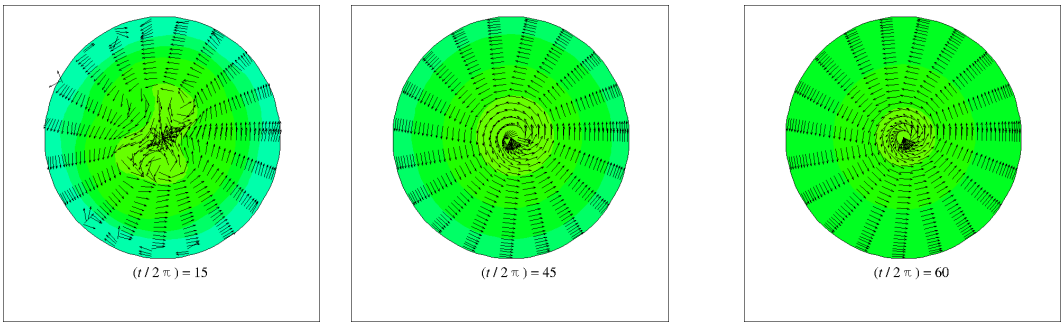


(c) $z = 0.9$

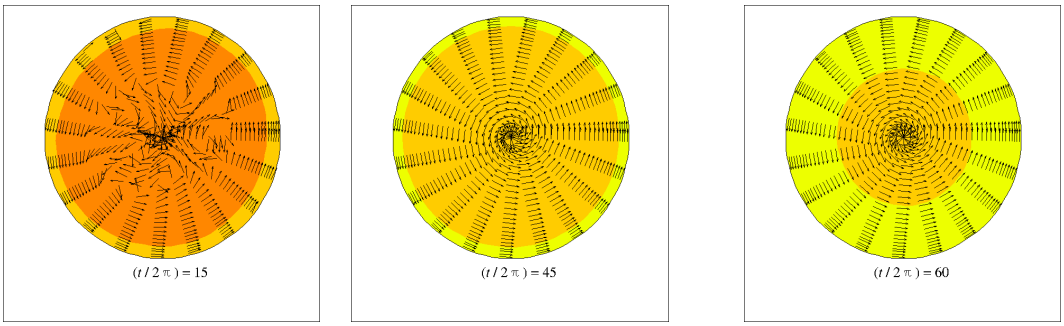


(d) Color Map

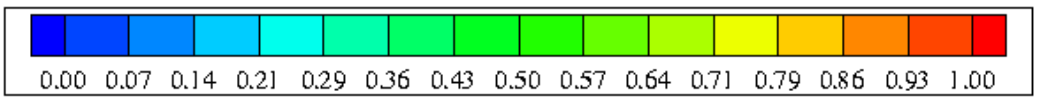


Figure 3.3: Plots of Temperature (Color Contours) and Baroclinic vorticity (Vectors) at different z-levels and times. The case is Neumann BC at $\Gamma = 2$ and $\varepsilon = 1.0$

Figure 3.4 above shows time dependent plots of temperature $\Theta$ at labeled radii. Oscillations observed at early time at $r = 1.0$ get damped at about $t/2\pi = 50$, though oscillations near bottom persist longer. Short containers ($\Gamma = 1.0, 2.0$) cannot produce large radial velocity. Hence the corner regions developed in these containers are shorter in z-direction as compared with long container ($\Gamma = 3.3$). This results in lower sloping of isotherms,

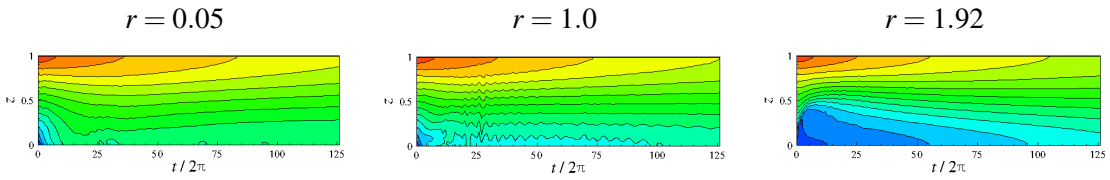


Figure 3.4: Plots of Temperature at different radii as a function of time. Same color plot used as above figure.

which fails to produce baroclinic disturbances that would cause loss of axisymmetry.

## 3.2 Unstable cases

Next are cases of third aspect ratio $\Gamma = 3.3$ shown in figure 3.5 and 3.6, where instabilities occurred.

(a) $\varepsilon = 0.5, \Gamma = 3.3$

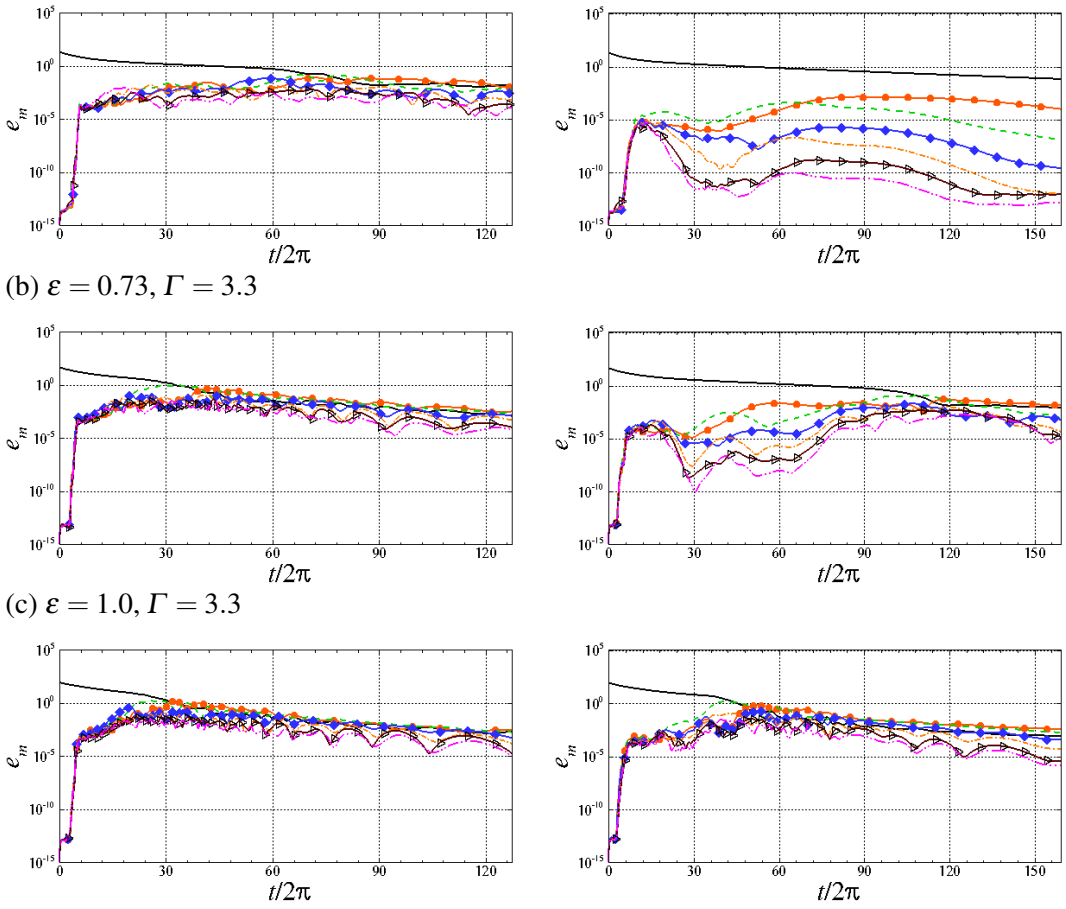


(b) $\varepsilon = 0.73, \Gamma = 3.3$




(c) $\varepsilon = 1.0, \Gamma = 3.3$




Figure 3.5: Time evolution of different energy modes $e_m$ at $\Gamma = 3.3$. The figures in the left column correspond to the spin-up with Neumann boundary conditions, and those in the right column to the Dirichlet boundary conditions. $m = 0$ (—— black); $m = 1$ (–○– red); $m = 2$ (– – green); $m = 3$ (–◇– blue); $m = 4$ (–·– orange); $m = 5$ (–▷– brown); $m = 6$ (–· ·– magenta).

The m-energy plots clearly show that $m = 1, 2, 3$ modes overtake the mean flow energy curve in all cases except for Dirichlet case with $\varepsilon = 0.5$. For higher $\varepsilon$ values the $m \neq 0$ modes overtake the mean current energy curve quickly. For Neumann cases flow becomes

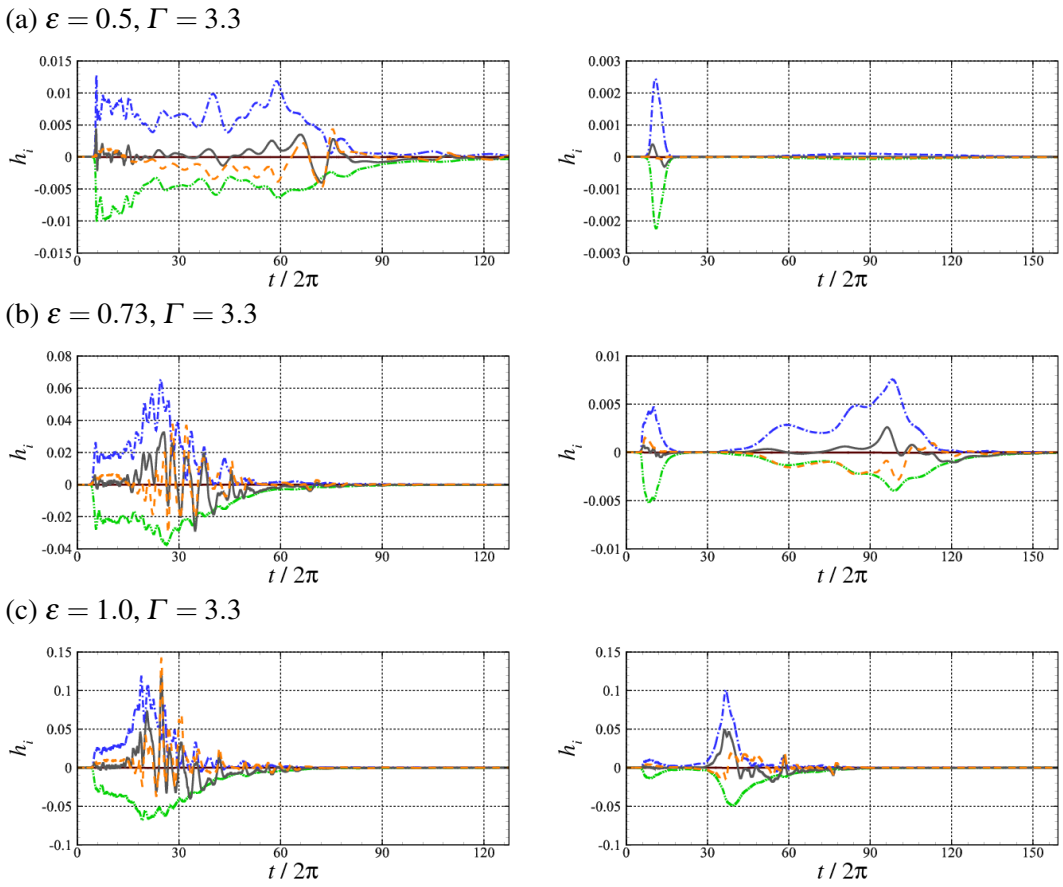


Figure 3.6: Time evolution of $h_i$-terms and the rate of change of kinetic energy of azimuthal perturbations. The figures in the left column correspond to the spin-up with Neumann boundary conditions, and those in the right column to the Dirichlet boundary conditions. Barotropic term $h_1$ (– – red); baroclinic term $h_2$ (– · – blue); centrifugal term $h_3$ (··· brown); viscous dissipation term $h_4$ (– · · · – green); rate of change of kinetic energy $\mathrm{d}e/\mathrm{d}t = \sum_i h_i$ (—- gray).

unstable at $(t/2\pi) = 75, 40, 30$ respectively for $\varepsilon = 0.5, 0.73, 1.0$. In case of Dirichlet cases unstable regime is reached at $(t/2\pi) = 105, 48$ for $\varepsilon = 0.73, 1.0$ Particularly at $\varepsilon = 0.5$ the flow loses axisymmetry at about $(t/2\pi) = 85$ but the central vortex core tries to regain the axisymmetry at the end. This is because the mean current tries to dominate in the later stages. Figure 3.6 shows the contributions from $(h_i)$ energy terms from equation 2.9. In all cases the barotropic term $h_2$ being initially positive serves the source of energy to perturbations. Both horizontal and vertical shears contribute to instability. The baroclinic and barotropic terms oscillate and act as source and sink correspondingly.

For Neumann cases the perturbations continue their growth and thus axisymmetry

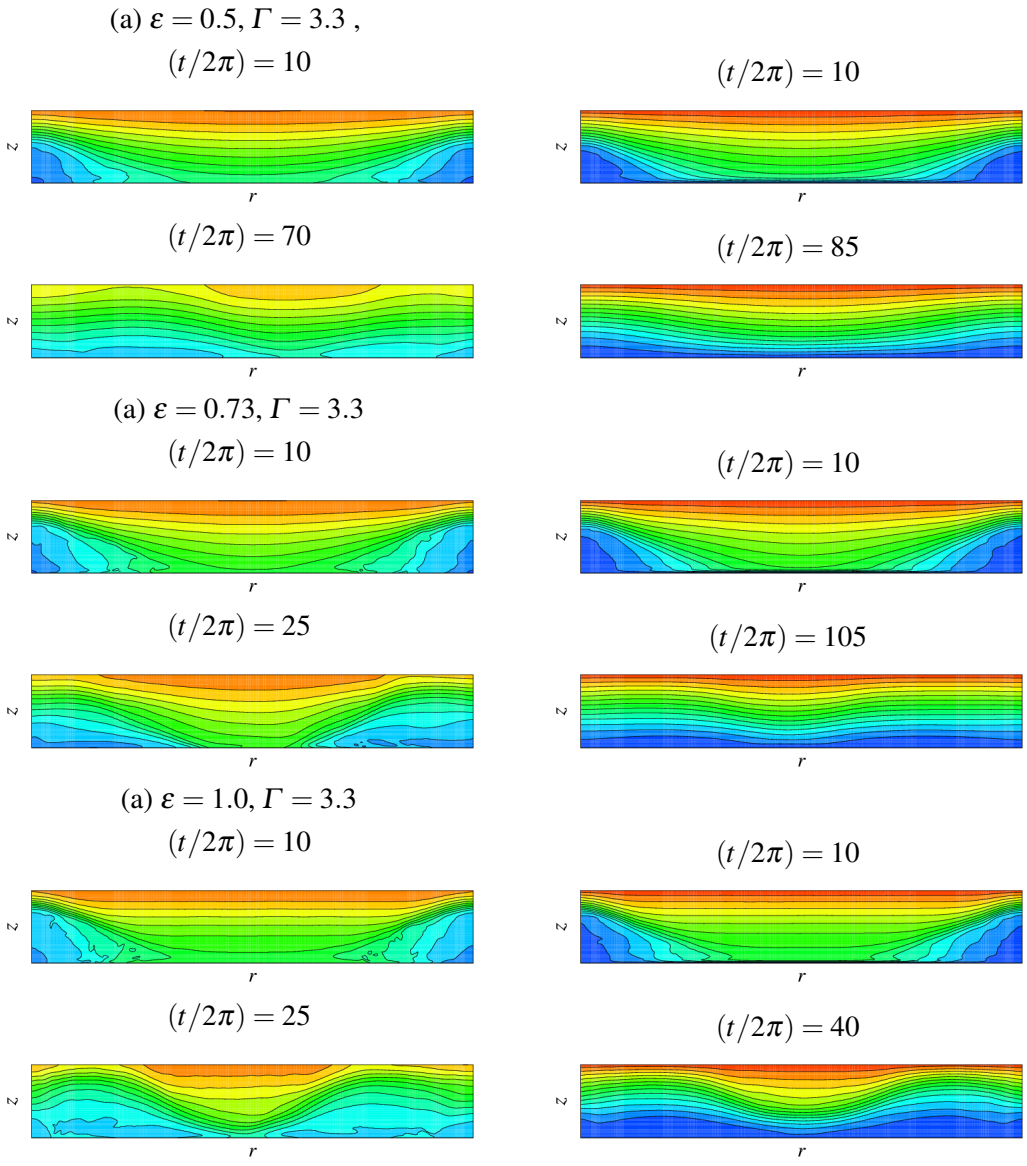


Figure 3.7: Plots of Isotherms at different times in $r-z$ plane at $0-\pi$ cross-section for unstable cases. 15 linearly spaced contour levels are used. Color plot in figure 3.10 show values of isotherms contours. Left column: Neumann BC cases and Right column : Dirichlet BC cases.

is lost quickly. Whereas in Dirichlet cases the perturbations lose energy after reaching initial local maximum and then again grow at late times. It can be observed that when this second growth exceeds the values of initial maximum the flow becomes unstable. Hence Dirichlet case with $\varepsilon = 0.5$ and $\Gamma = 3.3$ remained stable though it showed signs of loss of axisymmetry.

Figure 3.7 shows isotherms plots for Neumann and Dirichlet cases. These isotherm plots

illustrate the growth of corner regions thereby tilting of isotherms and oscillations due to internal waves generation.

These plots are isolines of temperature $\Theta$ in $r-z$ plane at different times. Again the same color plot is used as above for the contour levels. Plots at $(t/2\pi) = 10$ show the isotherms when corner regions mature. The plots at later times show the internal waves / oscillations generated. These waves can also be detected in figure 3.6 represented by oscillations of $h_i$ terms. From both of these plots 3.6 and 3.7 it can be seen that perturbations grew earlier in Neumann cases than Dirichlet cases. Smirnov *et al.* [2010*a*] observed this delayed rise of instability in Dirichlet BC configurations of their simulations. Simulations conducted herein confirmed that perturbation energy structure remains same for Dirichlet cases. All unstable cases showed initial local maximum followed by late baroclinic growth of perturbation energy. This structure can be observed for all $\varepsilon$ values. In upcoming section attention is given to find out mechanism behind this delayed instability.

## 3.3 Analysis of baroclinic vorticity dynamics for unstable Dirichlet cases.


Figure 3.8: Color plot used for the contour levels of baroclinic vorticity components.

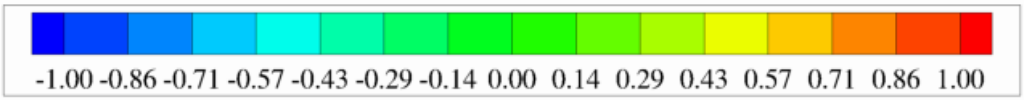


Figure 3.9: Color plot used for the contour levels of $\Omega_z$ vorticity (z-axis vorticity) component.

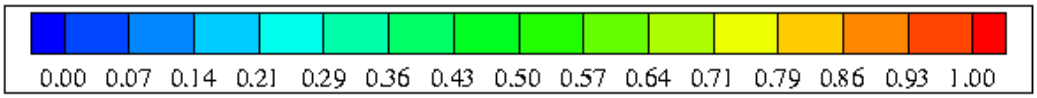


Figure 3.10: Color plot used for the contour levels of temperature $\Theta$.

It is known that spin-up process causes formation of Ekman layer at horizontal walls. In the case at hands there is Ekman layer formation at bottom. Ekman layer throws fluid at sidewall due to centrifugal force and in process draws fluid in through central core. This causes downwelling in central region and upwelling near the sidewalls. This causes tilting of isotherms in case of thermally stratified fluid. From equation 2.11, this tilting of isotherms causes the fourth term on RHS to become nonzero, giving rise to baroclinic source of vorticity. The dimensional form of this baroclinic vorticity in equation 2.12 indicates that it has two components viz. radial one and azimuthal one. The radial component has magnitude due to azimuthal temperature gradients and the azimuthal one has magnitude due to radial temperature gradients. Any azimuthal variation in temperature will lead to increase in shear and vorticity in vertical plane. The fact that vortex enhances the azimuthal

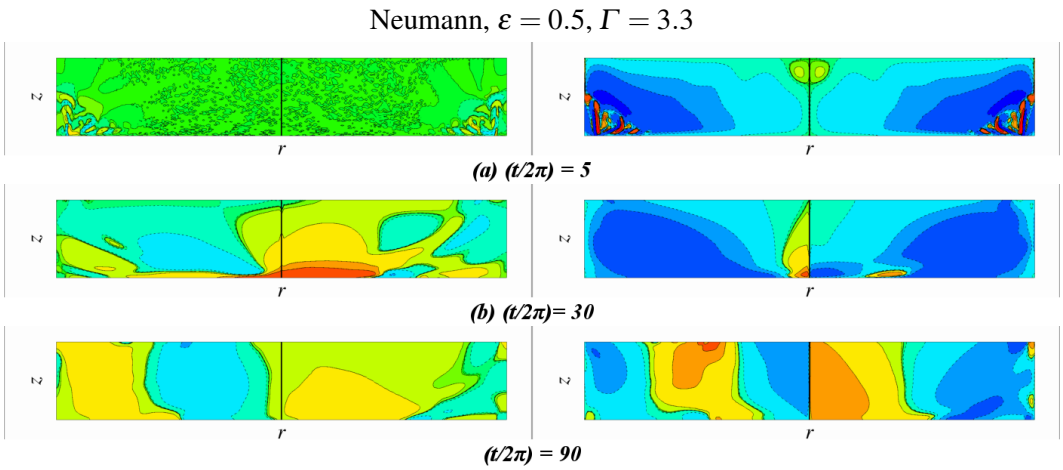


Figure 3.11: Plots of Baroclinic vorticity for Neumann case and labeled aspect ratio. Left hand column indicates Radial component of baroclinic vorticity and right hand column indicates azimuthal component of baroclinic vorticity.

temperature gradients which in turn reinforce the vortex, allows one to monitor baroclinic vorticity as a feedback that strengthens vortices. Strong stratification favors the stability of anticyclonic vortex allowing them to last long Peltier & Potylitsin [1998]. Thus with help of plots of two components in $r-z$ plane the baroclinic vorticity can be monitored as a feedback of azimuthal variation in temperature. These plots are followed by snaps of z-axis vorticity which give the idea of vertical vortex structures (cyclones and anticyclones).

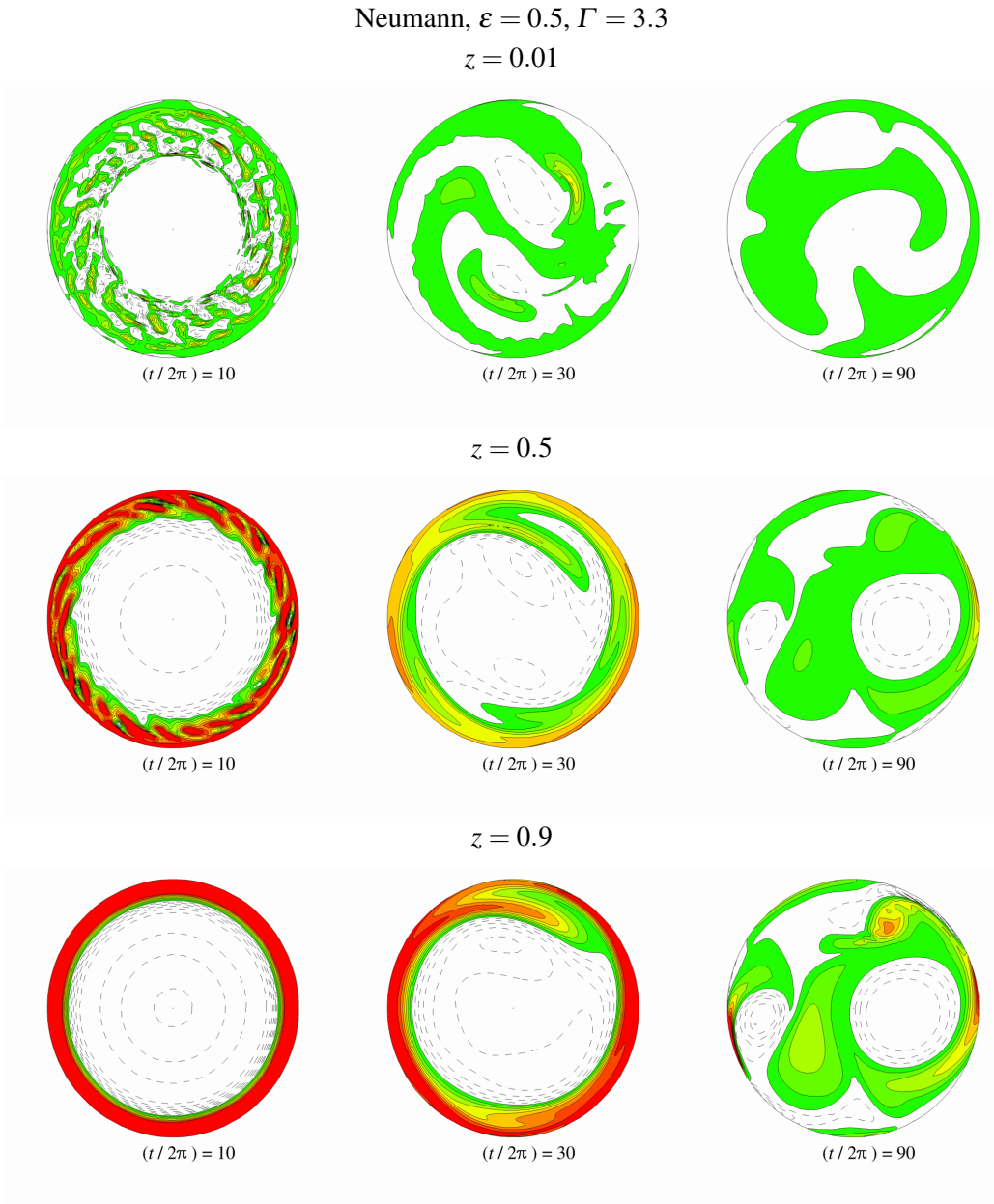


Figure 3.12: Contour plots of z-vorticity at different times and z-levels

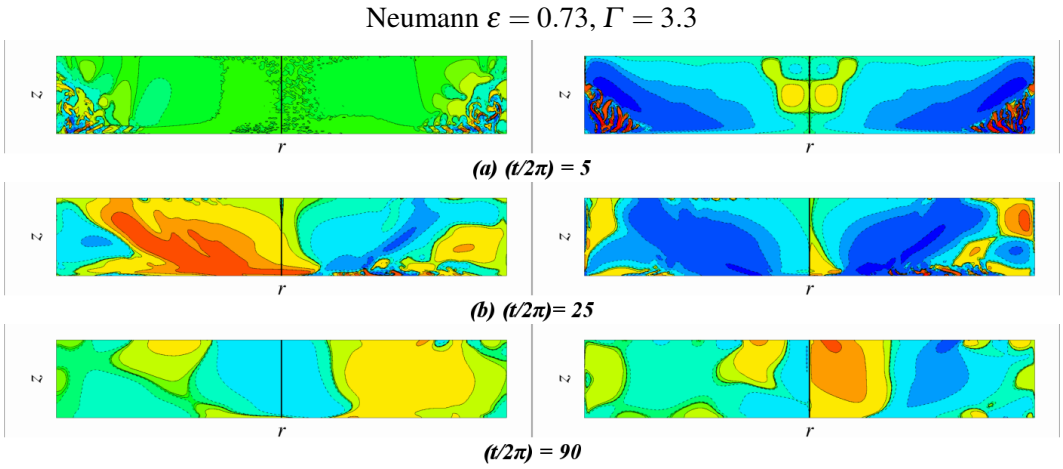


Figure 3.13: Plots of Baroclinic vorticity for Neumann case and labeled parameters. Left hand column indicates Radial component of baroclinic vorticity and right hand column indicates azimuthal component of baroclinic vorticity.

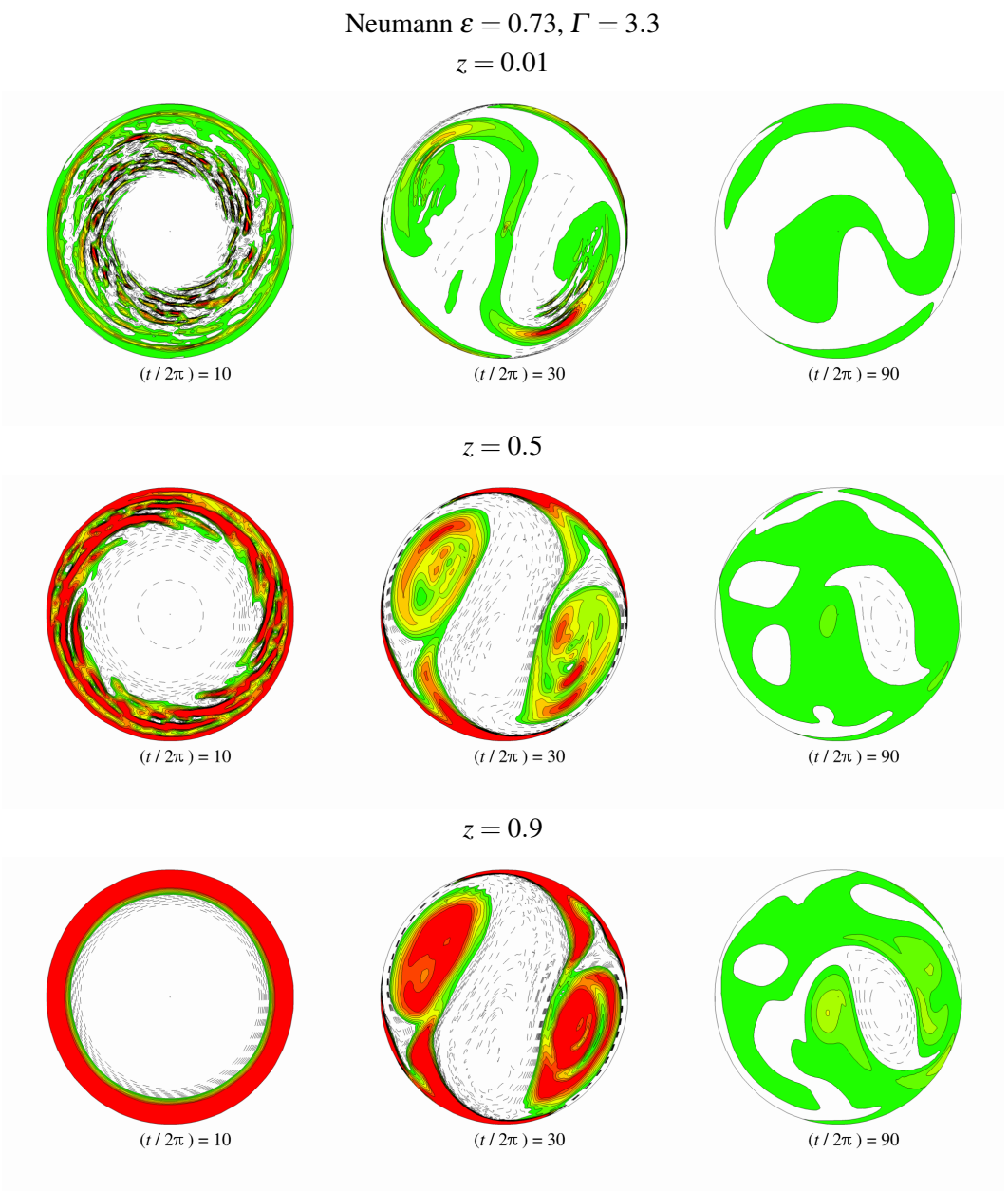


Figure 3.14: Contour plots of z-vorticity at different z-levels and times

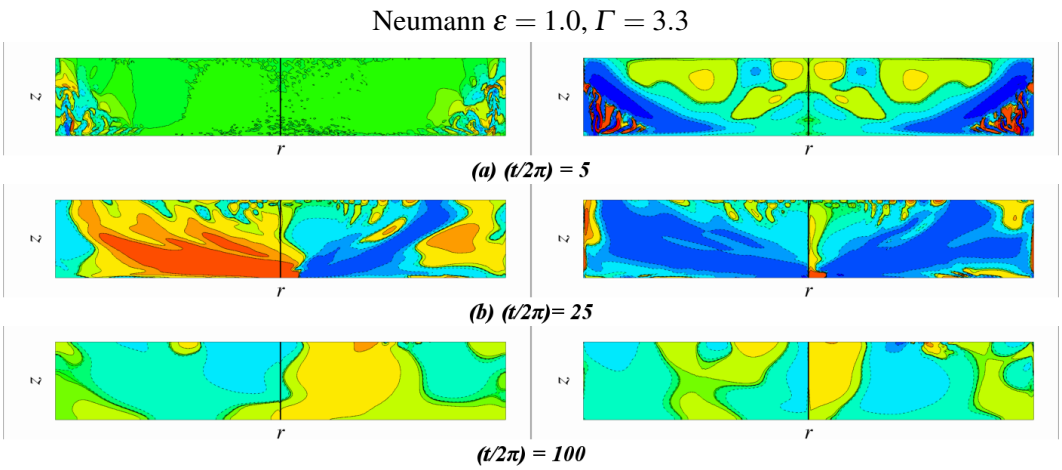


Figure 3.15: Plots of Baroclinic vorticity for Neumann case and labeled aspect ratio. Left hand column indicates Radial component of baroclinic vorticity and right hand column indicates azimuthal component of baroclinic vorticity.

Figures 3.11 to 3.16 are the plots for Neumann cases as labeled. At early times ($t/(2\pi) < 5$) there is only $\theta$ component of baroclinic vorticity indicating that radial temperature gradients dominate. Red spots in corner regions indicate huge radial variation in temperature caused by tilting of isotherms. The size of red spots is larger at higher $\varepsilon$ values. After ($t/(2\pi) > 10$) as corner regions stop growing the $r$-radial component of baroclinic vorticity starts showing higher values. When time reaches around ($t/(2\pi)$ 15), the reduced values of $\theta$ component indicate the collapse of corner regions. These plots are obtained approximately at times when local maximum of baroclinic term in $h_i$ energy terms plots occurs. Azimuthal baroclinic component plots depict the loss of axisymmetry, whereas radial component plots show development of azimuthal temperature gradients. All z-vorticity $\omega_z$ plots indicate the loss of axisymmetry and formation of cyclones (solid colored lines)and anticyclones (negative vorticity contours i.e. dotted lines with no coloring). Axisymmetry is lost earlier after collapse of corner regions. For all $\varepsilon$s the central vortex core disintegrates into cyclones and anticyclones. Plots at later times show that anticyclones last longer than cyclones which are disintegrated continuously. The baroclinic vorticity plots confirm this behavior.

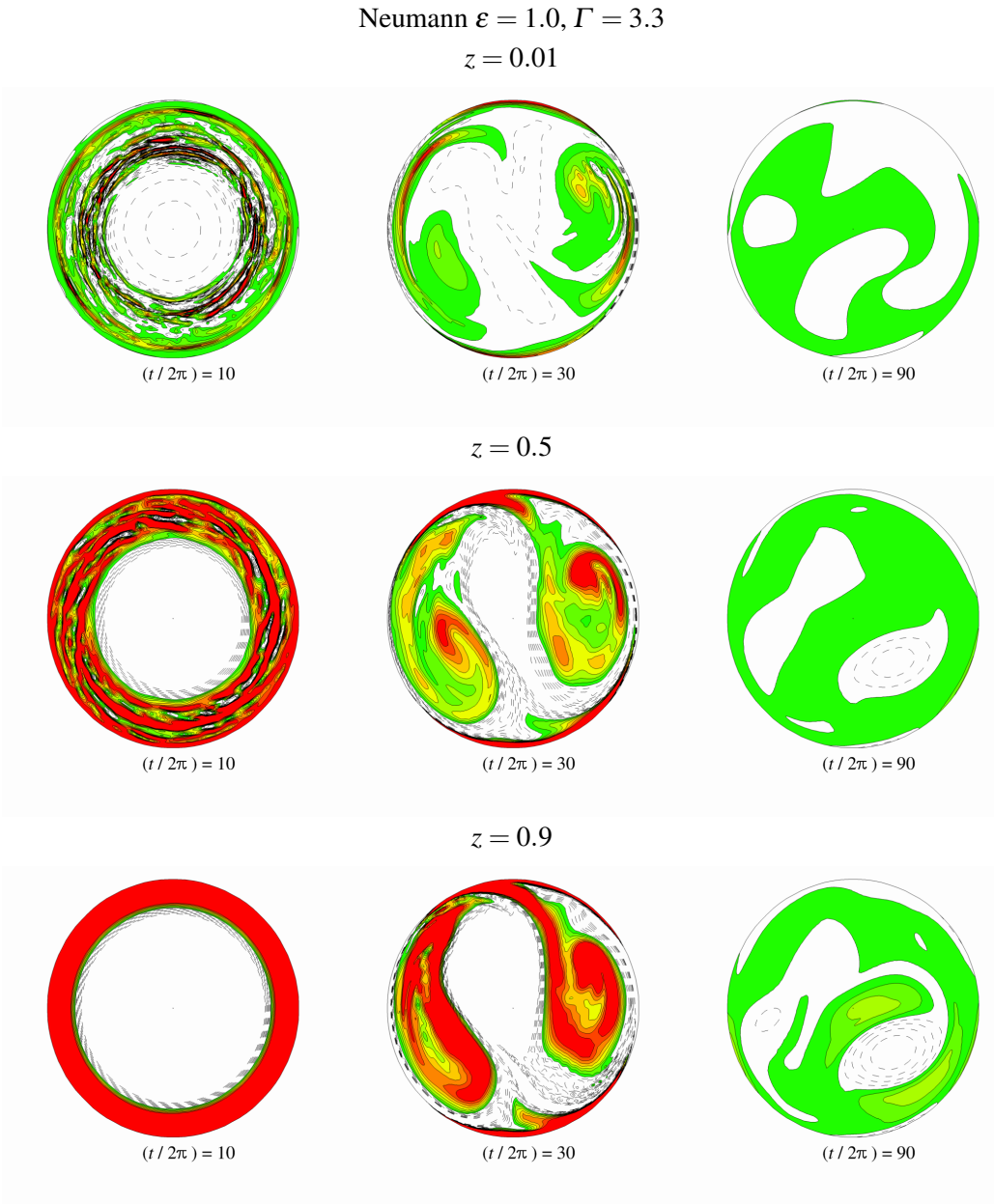


Figure 3.16: Contour plots of z-vorticity at different z-levels and times

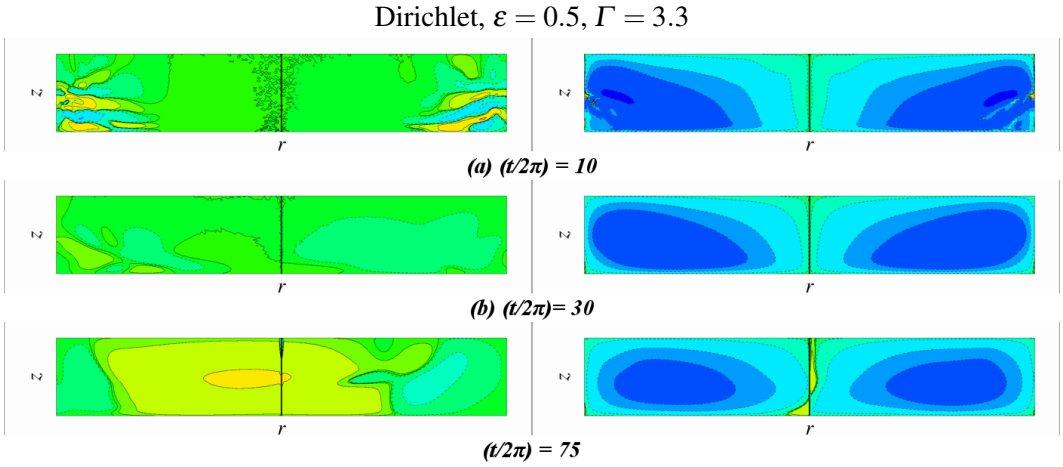


Figure 3.17: Plots of Baroclinic vorticity for Dirichlet case and labeled aspect ratio. Left hand column indicates Radial component of baroclinic vorticity and right hand column indicates azimuthal component of baroclinic vorticity.

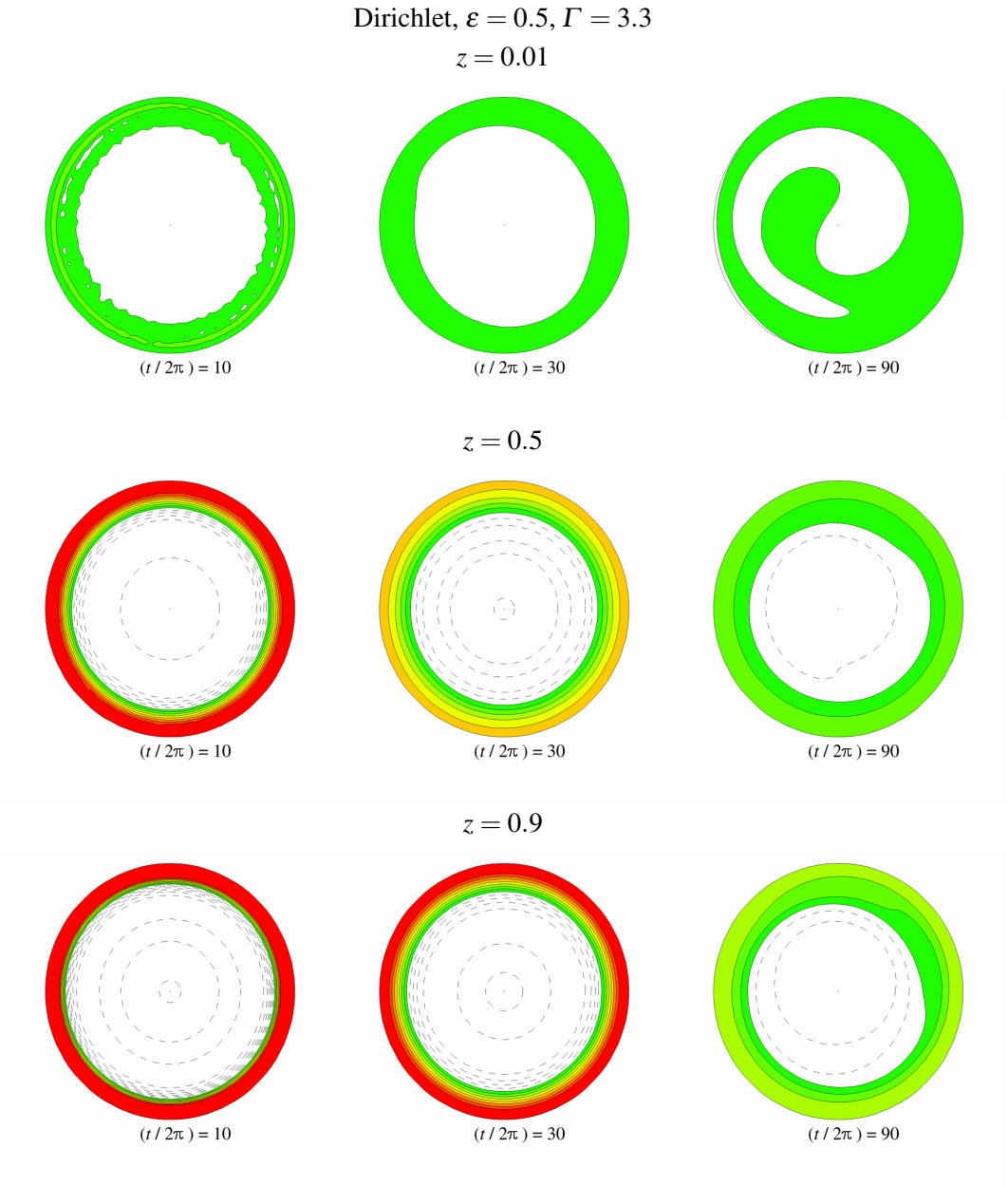


Figure 3.18: Contour plots of z-vorticity at different z-levels and times

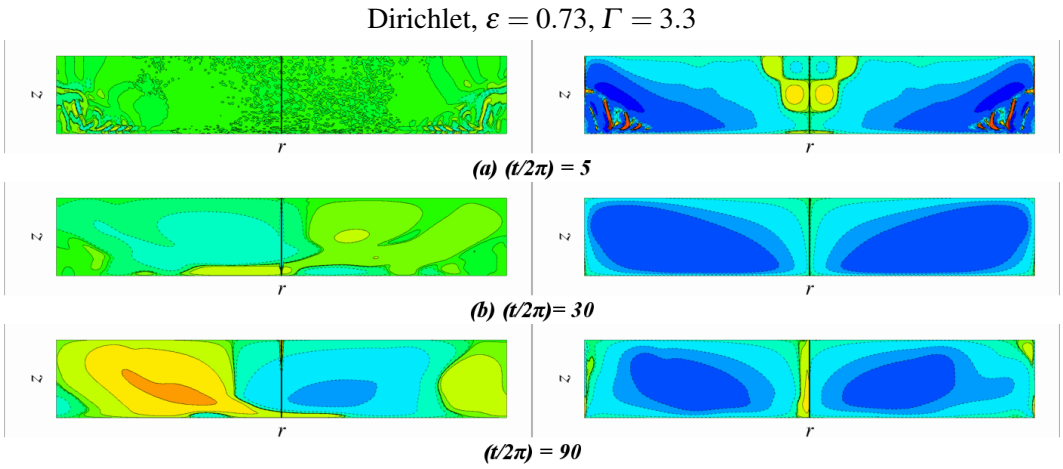


Figure 3.19: Plots of Baroclinic vorticity for Dirichlet case and labeled aspect ratio. Left hand column indicates Radial component of baroclinic vorticity and right hand column indicates azimuthal component of baroclinic vorticity.

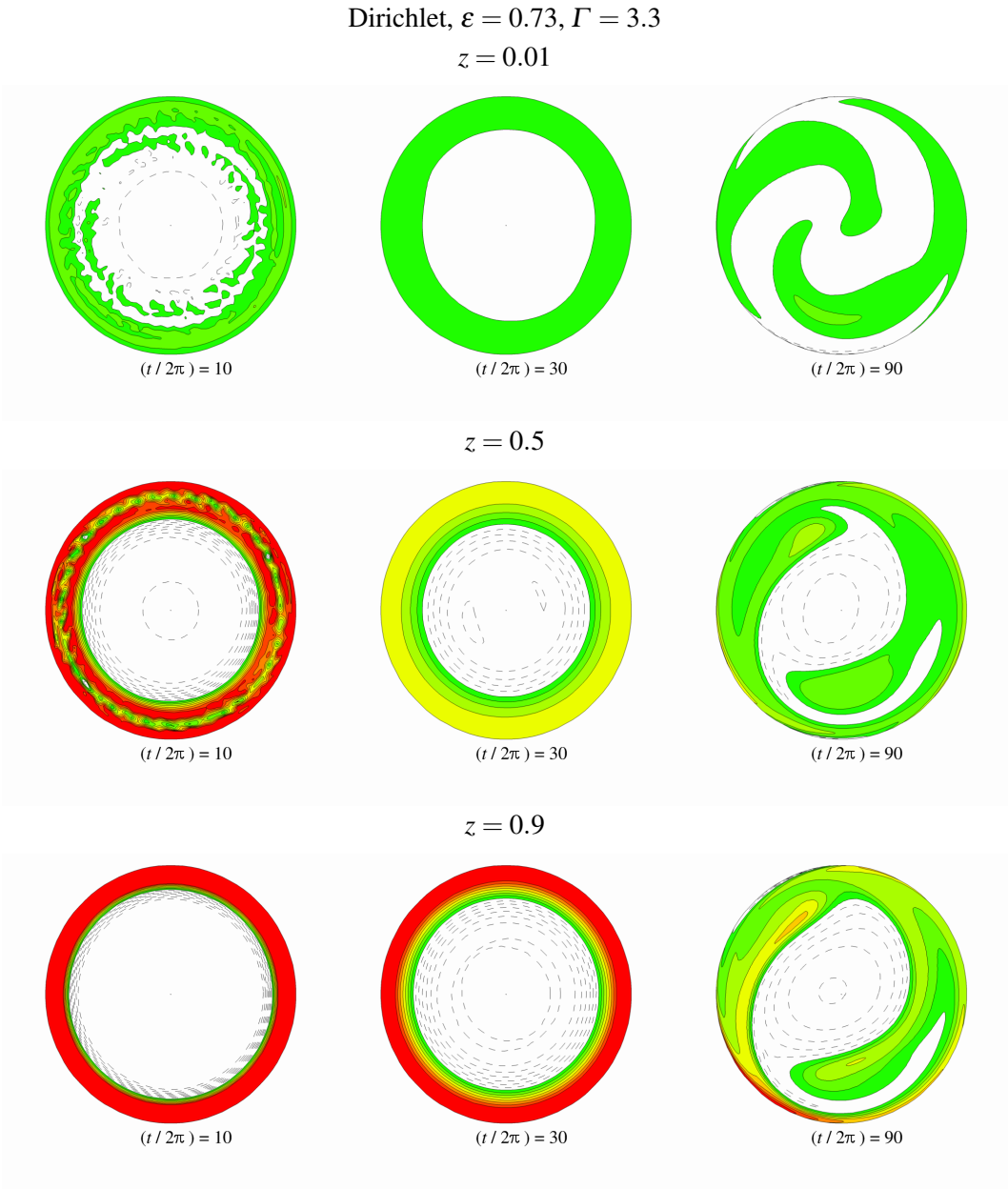


Figure 3.20: Contour plots of z-vorticity at different z-levels and times

On similar lines figures 3.17 to 3.22 are the plots of baroclinic vorticity components and z-vorticity snap-shots for Dirichlet cases which lost axisymmetry ($\Gamma = 3.3$). At ($\varepsilon = 0.5$) the azimuthal component of baroclinic vorticity remains uniform and axisymmetric which means corner regions are homogenized or isotherms are less tilted failing to create high radial temperature gradients. Even at around ($t/(2\pi) = 30$) after the corner regions collapse the radial component of vorticity shows small values. At late times ($t/(2\pi) \approx$

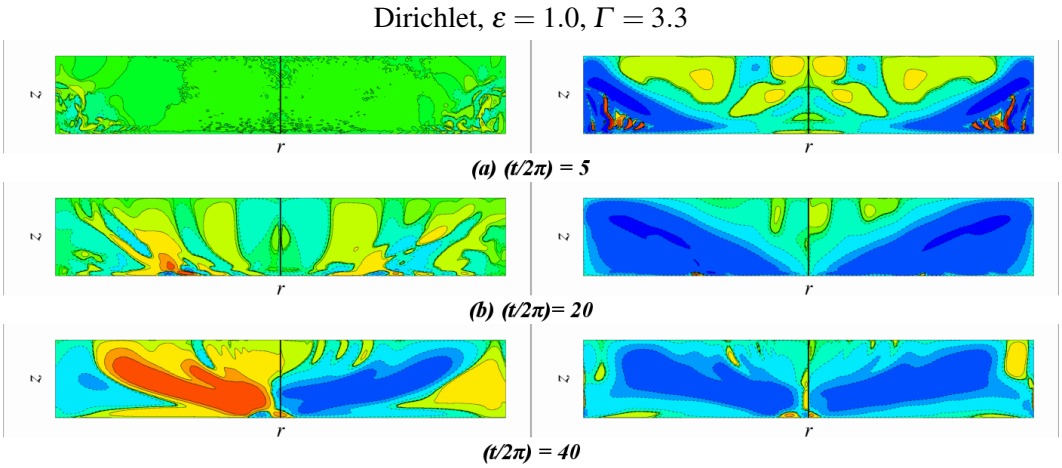


Figure 3.21: Plots of Baroclinic vorticity for Dirichlet case and labeled aspect ratio. Left hand column indicates Radial component of baroclinic vorticity and right hand column indicates azimuthal component of baroclinic vorticity.

75) this radial component shows some increased values and azimuthal component shows slight loss of axisymmetry. This is evident from late time plots of z-vorticity also. Next for $\varepsilon = 0.73$ the azimuthal baroclinic vorticity shows increased values (red spot) in the corner regions indicating considerable tilting of isotherms has occurred. Then after collapse of corner regions azimuthal component decreases maintaining the axisymmetry, whereas radial component shows increased values. After $(t/(2\pi) = 50)$ the radial component shows increased values and azimuthal component shows loss of axisymmetry. z-vorticity plots show that axisymmetry is lost as central vortex core starts rotating eccentrically. At later times $(t/(2\pi) > 90)$ the vortex core splits into smaller vortices. Next is the case for $\varepsilon = 1.0$ where same behavior is observed but this time radial component shows high values at from early time. Flow tries to regain the axisymmetry as shown by plot of azimuthal component at $(t/(2\pi) \approx 18)$, but quickly loses it shown by plots at $(t/(2\pi) = 40)$. About same time the vortex core disintegrates into smaller vortices as observed in z-vorticity plots.

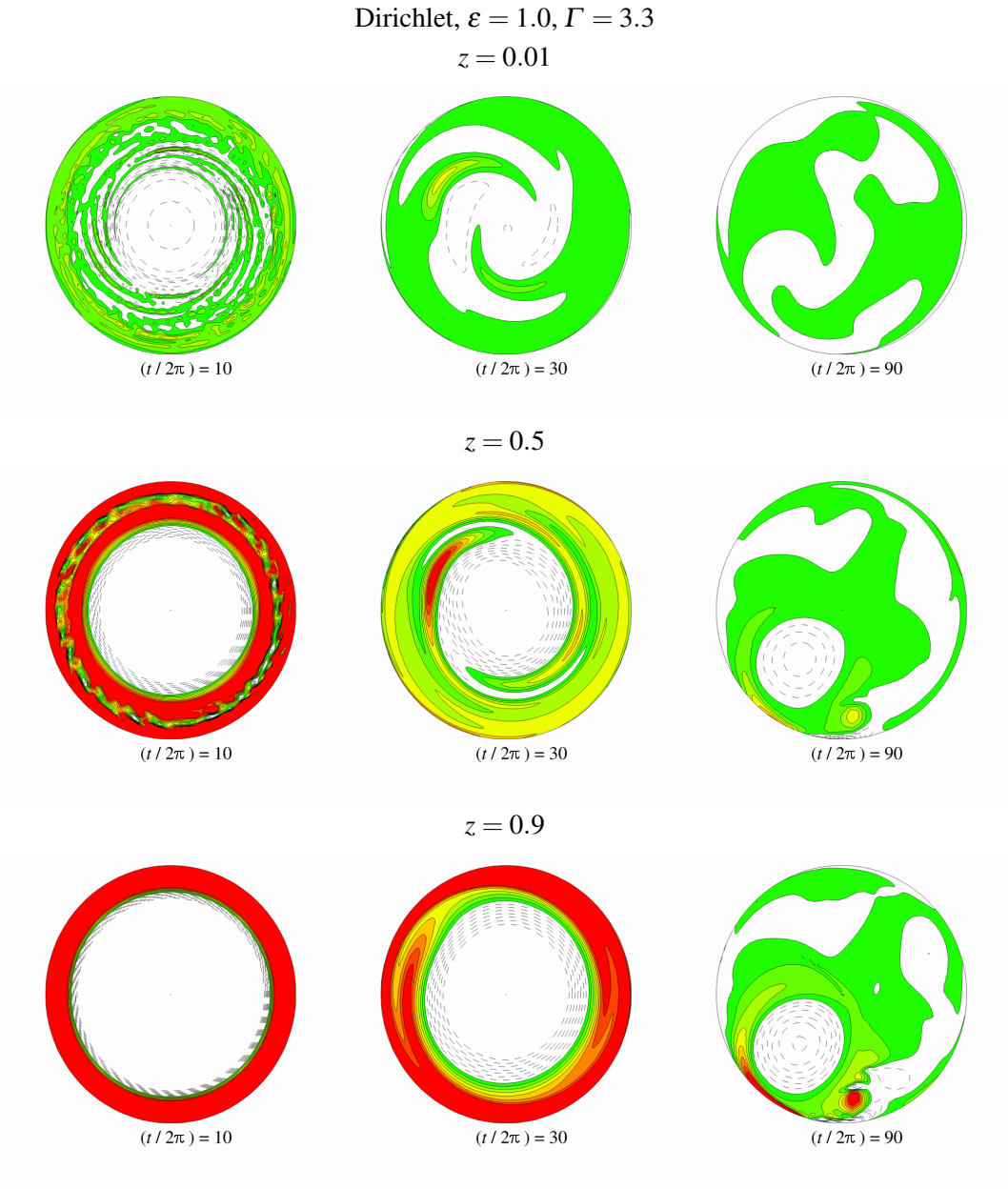


Figure 3.22: Contour plots of z-vorticity at different z-levels and times

Next from 3.23 to 3.25 are the plots of isotherms in $r - \theta$ plane at different z-levels at different times. In these plots dotted circle in black color line is shown for reference of axisymmetry. These plots support the observations of temperature gradients done through baroclinic vorticity plots. Initially radial temperature gradients exist due to Ekman pumping, shown by concentric rings of isotherms. But as the time progresses azimuthal temperature gradients develop along with loss of axisymmetry. In these plots also the axisymmetry

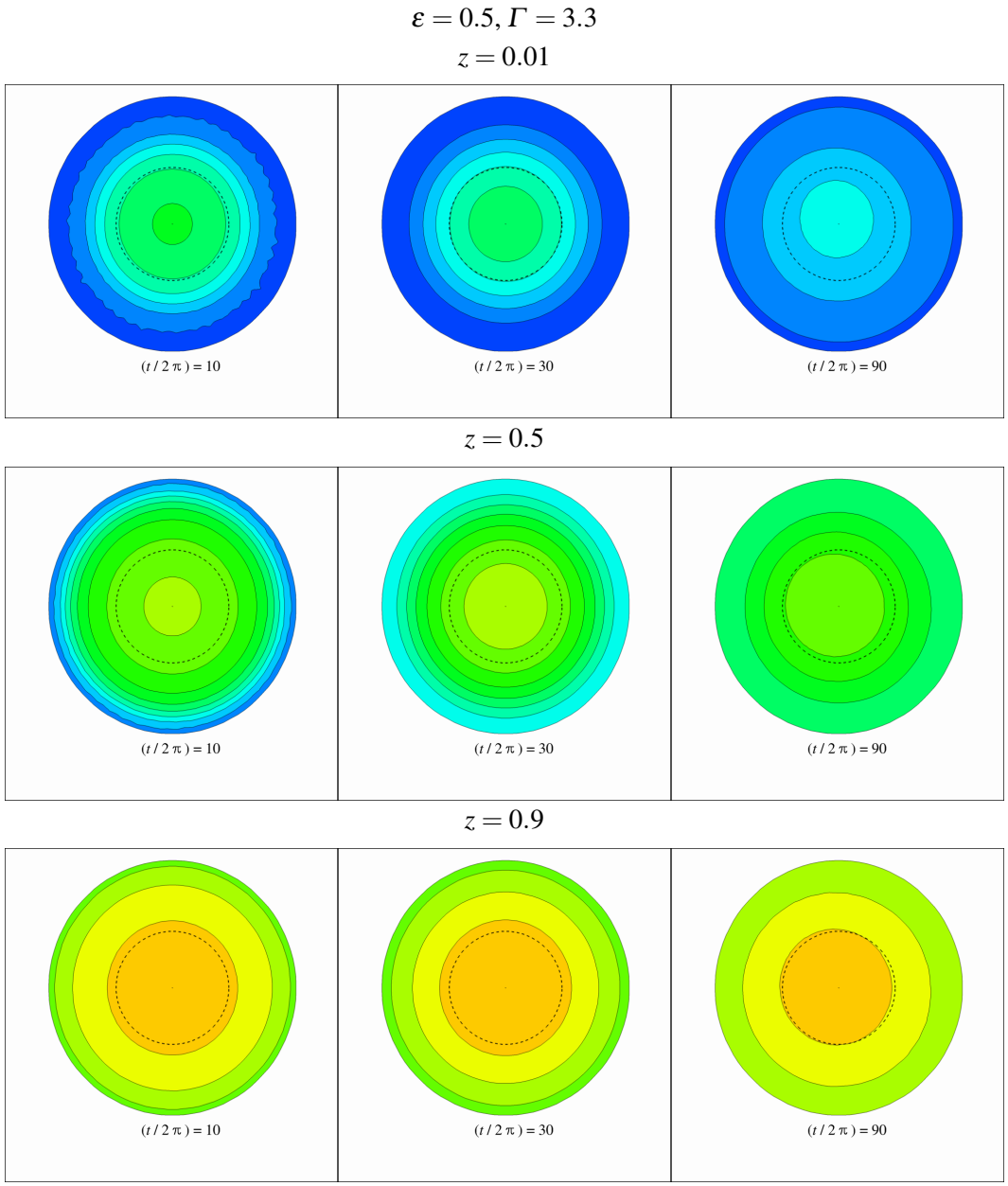


Figure 3.23: Contour plots isotherms at different z-levels and times

is lost via offset in the radius of concentric rings of isotherms. They start becoming elliptical at lower radii, and as the wobbling increases the vortex core starts getting stretched and disintegrates into smaller vortices. In addition figure 3.26 shows the time evolution of total kinetic energy of perturbations $e(t/(2\pi))$ from equation 2.9. These plots are generated by shutting off the baroclinic term at several different times for Dirichlet cases at $\Gamma = 3.3$ and $\varepsilon = 0.73, 1.0$. The energy curve decreases exponentially in both cases when baroclinic term

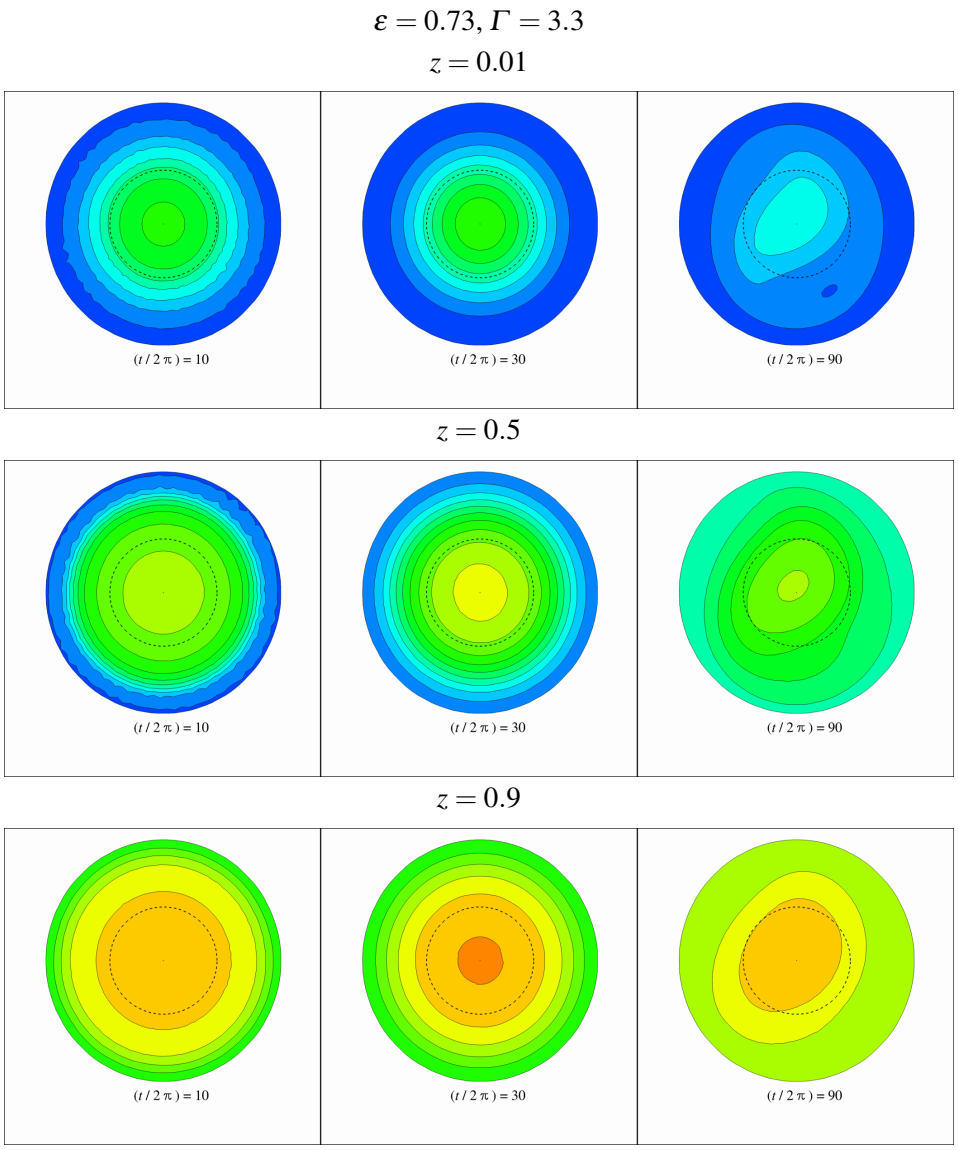


Figure 3.24: Contour plots of isotherms at different z-levels and times

is turned off. Otherwise it reaches maximum when perturbations gain energy from mean current and starts decaying as energetic phase of the flow comes to an end. This shows that for the Dirichlet cases the baroclinic term acts as a source of energy for perturbations and without it flow simply decays to quiescent phase without any instabilities.

The Dirichlet case with $\Gamma = 3.3$ and $\varepsilon = 0.73$ is ideal to analyze as it shows exactly how the delayed instability occurs. The perturbations induced due to truncational and computational errors, gain energy from initial shear imparted due to sudden change in rotation. The imposed temperature boundary conditions resist their growth and flow tries to stabilize with

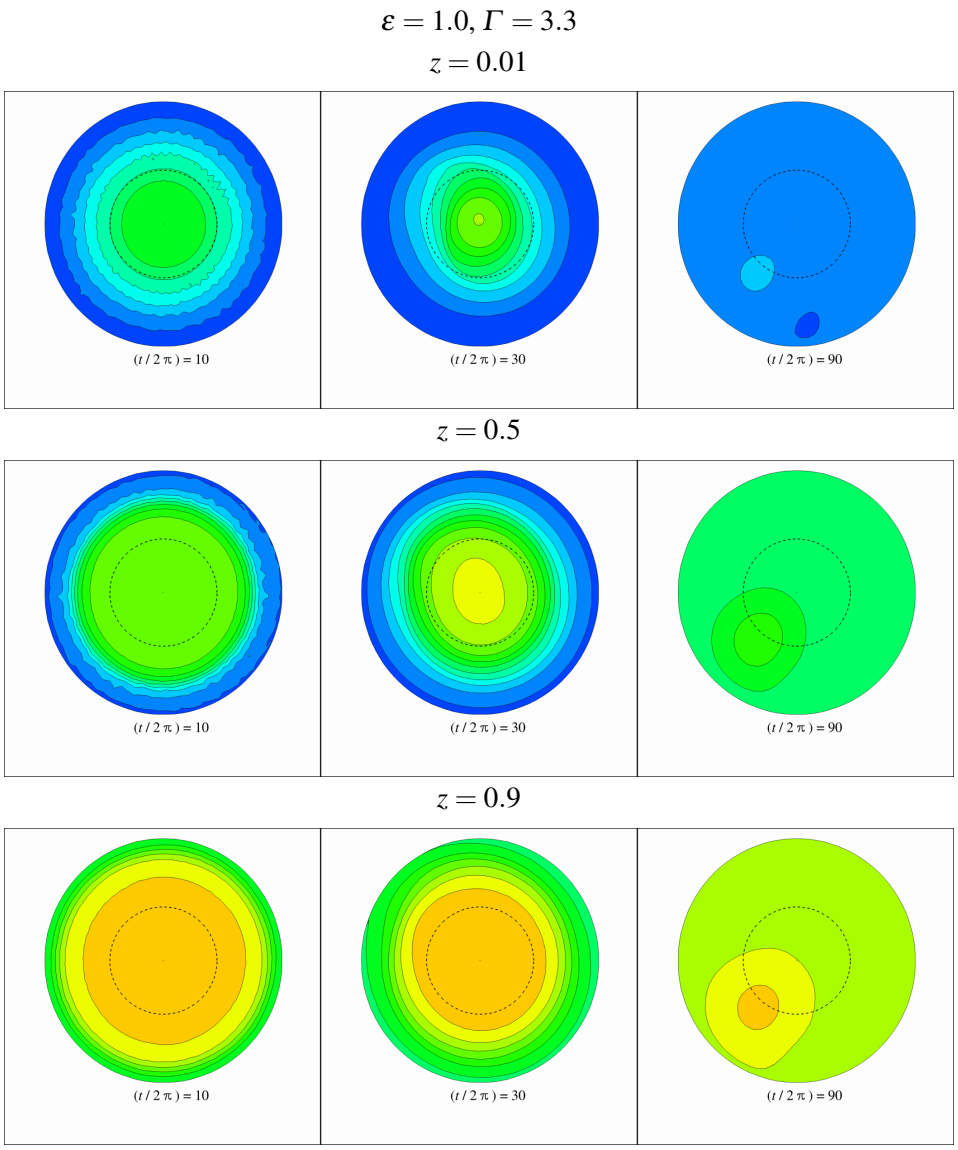


Figure 3.25: Contour plots of isotherms at different z-levels and times

efforts to gain axisymmetry. But vortices formed due to initial rise of perturbations and separation of corner region from central vortex core, enhance the azimuthal temperature gradients. Small amount of increase in azimuthal temperature gradients causes increase in radial component of baroclinic vorticity. This increases shears in vertical plane and make the central core vortex stronger. This feedback cycle continues and at one point baroclinic vorticity values become so high that vortex core starts deforming into an ellipse. This draws flow into unstable regime with perturbations reaching local maximum again this time gaining higher values than initial maximum. Thus the discussion of baroclinic vorticity feedback

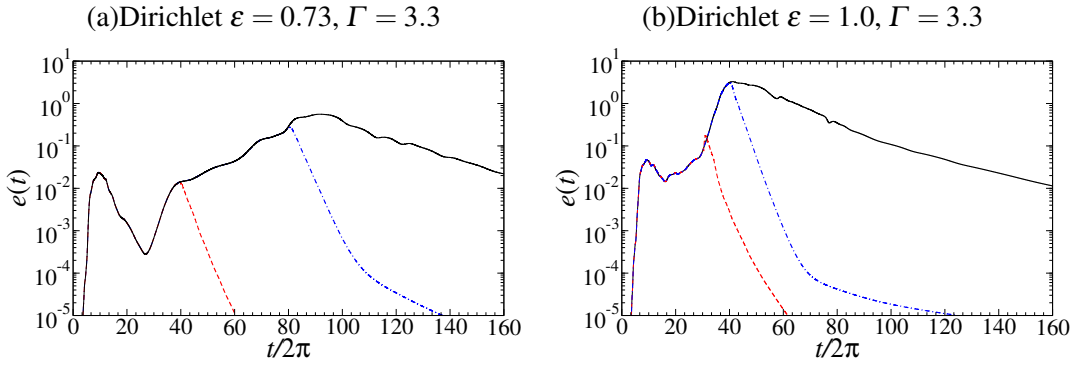


Figure 3.26: Plots of perturbation kinetic energy $e(t/2\pi)$ for Dirichlet cases at $\varepsilon = 0.73, 1.0, \Gamma = 3.3$. when baroclinic term is turned off (a) at $(t/2\pi) = 40$ $(--)$ ; $e(t/2\pi) = 80$ $(- \cdot -)$; $e(t/2\pi) \to \infty (- - - -)$ and (b)$(t/2\pi) = 30$ $(--)$ ; $e(t/2\pi) = 40$ $(- \cdot -)$;$e(t/2\pi) \to \infty (- - - -)$

mechanism can be ended at this point which serves the objective of this research.

Chapter 4

# CONCLUSIONS

The results of three dimensional transient numerical simulations of non-linear thermally stratified spin-up in a cylindrical geometry are presented in this dissertation. 18 simulations were performed with 9 Neumann thermal BCs cases and 9 Dirichlet thermal BC cases. Three aspect ratios were used ($\Gamma = 1.0, 2.0, 3.3$) with three Rossby numbers ($\varepsilon = 0.5, 0.73, 1.0$) at each one.

- **Results for short cylinders $\Gamma = 1.0, 2.0$ and $\varepsilon = 0.5, 0.73, 1.0$ show that tilting of isotherms is not in amounts which will lead to instability and loss of axisymmetry.**
- **For unstable cases the nature of interaction between different energy terms of perturbations was verified and found to be consistent with results of (Smirnov *et al.* [2010*a*].**
- **For Dirichlet cases as $\varepsilon$ value increased the time span between initial growth of perturbations and later instabilities considerably reduced.**

The model case of Dirichlet BCs at $\Gamma = 3.3$ and $\varepsilon = 0.73$ is used to frame the theory of baroclinic feedback mechanism. This mechanism can be summarized as follows.

- **Central vortex core initiates the development of azimuthal temperature gradients due to presence of perturbations.**
- **Azimuthal gradients in the temperatures, make the baroclinic term in the vorticity equation nonzero.**
- **The baroclinic term act as a source of vorticity that strengthens anticyclonic vortices by developing shears in vertical plane.**

- **Vortices help in mixing of fluid, thereby moving warm fluid from the inner region outward, and cold fluid from outer wall (transported due to Ekman transport) inward.**
- **This local advective heat transport further enhances azimuthal temperature gradients completing the feedback cycle.**

As a future scope, one can study the behavior of cyclones by conducting spin-down experiments with the same parameters. This will throw some more light on application of this theory. So far these simulations are done with similar types of thermal boundary conditions, hence there is a possibility of implementing combination of two types of boundary conditions. (Dirichlet at top wall and Neumann at bottom wall; vice versa.) One of the assumptions which is shear free surface at top, might have some role in simulations, hence experiments should be conducted can be done in order to verify the theory. This will aid to quantify the analysis by monitoring certain variables to define or derive clear criterion for instability. In order to identify the role of sidewall boundary layers in these cases, one can conduct simulations with slip-sidewall with same parameters.

REFERENCES

ALLEN, J. S. 1973 Upwelling and Coastal Jets in a Continuously Stratified Ocean. *J. Phys. Ocean.* **3**, 245–257. 1

BENTON, E. R. & CLARK, A. 1974 Spin-up. *Ann. Rev. Fluid Mech.* **6**, 257–280. 1, 7

BOYER, D. L., SOUS, D. & SOMMERIA, J. 2009 Laboratory Experiments on Along-slope Flows in Homogeneous and Stratified Rotating Fluids. *Dyn. Atmos. Oceans* **46**, 19–35. 1

DUCK, P. W. & FOSTER, M. R. 2001 Spin-up of Homogeneous and Stratified Fluids. *Ann. Rev. Fluid Mech.* **33**, 231–263. 1

FLÓR, J.-B., BUSH, J. W. M. & UNGARISH, M. 2004 An Experimental Investigation of Spin-up from Rest of a Stratified Fluid. *Geophys. Fluid Dyn.* **98**, 277–296. 2

FLÓR, J.-B., UNGARISH, M. & BUSH, J. W. M. 2002 Spin-up from Rest in a Stratified Fluid: Boundary Flows. *J. Fluid Mech.* **472**, 51–82. 1

GARRETT, C., MACCREADY, P. & RHINES, P. 1993 Boundary Mixing and Arrested Ekman Layers: Rotating Stratified Flow Near a Sloping Boundary. *Ann. Rev. Fluid Mech.* **25**, 291–323. 1

GILL, A. E. 1982 *Atmosphere-ocean Dynamics*. San Diego, CA: Academic Press. 5

GREENSPAN, H. P. 1968 *The Theory of Rotating Fluids*. Cambridge, U.K.: Cambridge University Press. 1

GREENSPAN, H. P. 1980 A Note on the Spin-up from Rest of a Stratified Fluid. *Geophys. Fluid Dyn.* **15**, 1–5. 2

HALLWORTH, M. A., HUPPERT, H. E. & UNGARISH, M. 2001 Axisymmetric Gravity Currents in a Rotating System: Experimental and Numerical Investigations. *J. Fluid Mech.* **447**, 1–29. 1

HUNT, J. C. R., PACHECO, J. R., MAHALOV, A. & FERNANDO, H. J. S. 2005 Effects of Rotation and Sloping Terrain on the Fronts of Density Currents. *J. Fluid Mech.* **537**, 285–315. 1

HYUN, J. M., FOWLIS, W. W. & A.WARN-VARNAS 1982 Numerical Solutions for the

Spin-up of a Stratified Fluid. *J. Fluid Mech.* **117**, 71–90. 10, 11

KANDA, I. 2004 A Laboratory Study of Columnar Baroclinic Vortices in a Continuously Stratified Fuid. *Dyn. Atmos. Oceans* **38**, 69–92. 2

LINDEN, P. F. & VAN HEIJST, G. J. F. 1984 Two-layer Spin-up and Frontogenesis. *J. Fluid Mech.* **143**, 69–94. 1

MAHALOV, A., PACHECO, J. R., VOROPAYEV, S. I., FERNANDO, H. J. S & HUNT, J. C. R. 2000 Effects of Rotation on Fronts of Density Currents. *Phys. Lett. A* **270**, 149–156. 1

MANLEY, T. O. & HUNKINS, H. 1985 Mesoscale Eddies of the Arctic Ocean. *J. Geophys. Res.* **90**, 4911–4930. 1

MCWILLIAMS, J. C. 1985 Submesoscale, Coherent Vortices in the Ocean. *Geophys. Rev.* **23**, 165–182. 1

MOULING, F. Y. & FLÓR, J.-B. 2004 On the Spin-up by a Rotating Disk in a Rotating Stratified Fluid. *J. Fluid Mech.* **516**, 155–180. 1

OLSON, D. B. 1991 Rings in the ocean. *Annu. Rev. Eartch Planet. Sci.* **19**, 283–311. 1

PACHECO, J. R., LOPEZ, J. M. & MARQUES, F. 2011 Pinning of Rotating Waves to Defects in Finite Taylor–Couette Flow. *J. Fluid Mech.* **666**, 254–272. 10

PELTIER, W. R. & POTYLITSIN, P. G. 1998 Stratification Effects on the Stability of Columnar Vortices on the F-plane. *J. Fluid Mech.* **355**, 45–79. 21

SMIRNOV, S. A., BOYER, D. L. & BAINES, P. G. 2005 Nonaxisymmetric Effects of Stratified Spin-up in an Axisymmetric Annular Channel. *Phys. Fluids* **17**, 086601. 2

SMIRNOV, S. A., PACHECO, J. R. & VERZICCO, R. 2010*a* Numerical Simulations of Nonlinear Thermally Stratified Spin-up in a Circular Cylinder. *Phys. Fluids* **22** (11), 116602. i, 2, 3, 8, 9, 10, 20, 37

SMIRNOV, S. A., PACHECO, J. R. & VERZICCO, R. 2010*b* Three-dimensional Vortex Visualization in Stratified Spin-up. *J. Visualisation* **13** (2), 81–84. 10

THOMAS, L. N. & RHINES, P. B. 2002 Nonlinear Stratified Spin-up. *J. Fluid Mech.* **473**,

211–244. 1

UNGARISH, M. & MANG, J. 2003 The Flow Field and Bare-spot Formation in Spin-up from Rest of a Two-layer Fluid About a Vertical Axis. *J. Fluid Mech.* **474**, 117–145. 1

VERZICCO, R. & CAMUSSI, R. 1997 Transitional Regimes of Low-Prandtl Thermal Convection in a Cylindrical Cell. *Phys. Fluids* **9**, 1287–1295. 10

VERZICCO, R., LALLI, F. & CAMPANA, E. 1997 Dynamics of Baroclinic Vortices in a Rotating Stratified Fluid: A Numerical Study. *Phys. Fluids* **9**, 419–432. 8, 10

VERZICCO, R. & ORLANDI, P. 1996 A Finite-difference Scheme for Three-dimensional Incompressible Flows in Cylindrical Co-ordinates. *J. Comput. Phys.* **123**, 402–414. 10